The Dissertation Committee for Yen-Yu Chang
certifies that this is the approved version of the following dissertation:

Single-Shot Diagnostics of Laser Driven Plasma Accelerators

Committee:

Micheal Downer, Supervisor

Manfred Fink

Boris Breizman

Michael Becker

Aaron Bernstein

Single-Shot Diagnostics of Laser Driven Plasma Accelerators

by

Yen-Yu Chang

DISSERTATION

Presented to the Faculty of the Graduate School of

The University of Texas at Austin

in Partial Fulfillment

of the Requirements

for the Degree of

DOCTOR OF PHILOSOPHY

THE UNIVERSITY OF TEXAS AT AUSTIN

August 2018

To my lovely family

Acknowledgments

I knew studying abroad would be an adventure, but I didn't expect this wonderful journey where I grew so much in so many aspects. I'm grateful for all the people I've encountered in the U.S., especially those who are always around me and support me. I wouldn't have accomplished the doctorate program without any of your help, so thank you.

First of all, I want to thank my family for always supporting me. I would like to thank my parents, who always listen to my problems, care for my situations, and encourage me to move forward. I cannot imagine how I could survive in this foreign country without their support. In addition, I want to thank my sister for taking care of my parents and everything in the family. Because of her, I can study and do research in the U.S. without worrying about my family too much.

Furthermore, I would like to thank all the members and previous members in Downer's research group. Dr. Downer has been supportive from the very beginning. He paid my ESL class tuition even before my first semester began. He was patient when I kept making stupid mistakes, and he was tolerant when I was offensive. He always shows acute insights in physics and resolves to discover the truth. I couldn't ask for a better mentor. Moreover, I would like to thank Rafael Zgadzaj. If there is such a thing as an experimen-

tal genius, then Rafael would be a perfect example. Almost all the innovative designs in my experiments are Rafael's idea. He always looks at the problems with a fresh mind and provides brilliant solutions immediately. His so observant that sometimes I'm afraid to show him my data analysis because he can always points out my mistakes right away. However, Rafael is very supportive, and without his advice, I could never resolve all the difficulties I encountered during my research. I also want to thank Aaron Bernstein for always giving me valuable guidance, Watson Henderson for instructing me how to machine home-made parts, Xiaoming Wang for fixing the laser system when I screwed up, Zhengyan Li for developing the foundation of frequency domain diagnostic techniques, Hai-En Tsai for showing me how to be a responsible scientist, Rick Korzekwa for forgiving me when I messed up his measurement, Joseph Shaw for all the help and encouragements, Kathleen Weichman for all the helpful conversations and discussions, and all the members in Downer's research group.

Single-Shot Diagnostics of Laser Driven Plasma Accelerators

Publication No. _____

Yen-Yu Chang, Ph.D.
The University of Texas at Austin, 2018

Supervisor: Micheal Downer

We demonstrated single shot diagnostics of laser-plasma accelerators (LPAs). We observed the structure and the evolving process of the blow-out region, the nonlinear waves (plasma bubble) induced by the driving beam using the Faraday rotation diagnostic. We obt ained the evolution of the plasma bubble in single shot using Faraday rotation diagnostic with multiple probe beams. The diameter of the bubble changed from 300 μm to 50 μm in 2 cm, which revealed the transition of the acceleration stages from "bubble expanding mode" to "bubble stabilizing mode". Moreover, we demonstrated the broad bandwidth frequency domain streak camera (B-FDSC), which can resolve the dynamics of LPAs in single shot. We improved the temporal resolution of B-FDSC to $\sim$ 10 fs by broadening the bandwidth of the probe beam to $\sim$ 100 nm using supercontinuum generation, and we performed a prototype

experiment to show that B-FDSC was capable of resolving the evolution of pulse self-steepening and temporal splitting in a single shot.

Table of Contents

List of Tables

List of Figures

Chapter 1

Introduction

1.1 Laser-Plasma Accelerators (LPAs) And The Bubble Regime

Since its inception in 1979[1], laser driven plasma accelerators (LPAs) have attracted wide interest as a tabletop radiation source. Several researchers have demonstrated that LPAs are capable of producing widely applicable radiation in a compact setup. For instance, Wang *et al.* [2] have accelerated electrons to more than 2 GeV, where the LPA was driven by high power laser delivered by the Texas Petawatt (TX PW), in a 10 cm long, Helium filled gas cell. Tsai *et al.* [3] also demonstrated that utilizing plasma mirror at the end of LPAs, in this case a 3 mm long gas jet, could produce tunable, ultrafast hard X-rays. Such radiations are application in biology, medicine, and materials science.

The compact size of LPAs is due to the unprecedented accelerating field (GeV/cm), contained in a light-speed, microscopic ($\sim 10^{-5}$ m) plasma structure, in comparison to the conventional metal cavity ($\sim$ 1 m) radio-frequency accelerators. When an intense laser pulse propagates through gas, the front of the pulse ionizes the gas and generates plasma, and the rest of the pulse induces a plasma wave that can sustain strong electric fields of gigavolts

per centimeters. The charged particles have been trapped can be accelerated by riding on the plasma wave. In particular, the LPAs operate best when the laser pulse is intense enough to blow out the ambient electrons to create an ion cavity, or plasma bubble. This is the so-called bubble regime.

The bubble regime was first proposed by Pukhov *et al.* [4] in 2002. Since then, several analytical studies of the bubble structures were developed[5][6][7]. In particular, Lu *et al.* [8] concluded that the key to generating plasma bubbles is that the driving beam needs to be intense enough to cause the expelled electrons to experience trajectory crossing. When the radius of the bubble reaches a certain level, the self-injection starts to occur. However, researchers have not reached a consensus on the appropriate criterion for the threshold of self-injection in terms of the bubble radius [7][9] [10]. Although the injection threshold has been tested experimentally [11] [12] by varying the initial parameters of the driving pulses, it would be better to measure and determine the self-injection threshold of R_b experimentally.

The dynamics of the plasma bubble are essential to the acceleration process. Simulations have shown that the plasma bubble experiences length contraction during self-injection. Kalmykov *et al.* [13] has suggested that the expansion rate of the plasma bubble has to exceed certain values to induce self-injection. Kalmykove *et al.* [14] has also reported that in a single-staged GeV-class LPA, the plasma bubbles can experience two phases in the acceleration process. In the first phase, when the driving pulse enters the plasma, the intensity of the pulse oscillates until the spot size matches the self-guiding

conditions. During the intensity oscillations, the bubble expands when the intensity of the drive pulse starts to decrease after non-linear focus, which leads to periodic self-injection. In the second phase, the bubble structure stabilizes and the driving pulse starts to experience temporal compression [15] and etching effects [16]. The self-injection stops when the bubble stops expanding. The bubble structures and bubble dynamics of GeV-class LPAs, however, have not been experimentally characterized due to low plasma density ($\sim 5 \times 10^{17}$ cm^{-3}) and long laser plasma interaction length (~ 10 cm).

1.2 Diagnostics of LPAs In High Density Plasma

Diagnostics of LPAs are essential to understanding the physics of the acceleration process. Researchers have used various techniques to study wake-field oscillation, self-injection, bubble formation. In particular, single shot techniques are preferential because of the shot-to-shot fluctuation of the laser systems and the non-linear laser plasma interaction.

There are plenty of diagnostics developed for high density ($\sim 1 \times 10^{19}$ cm^{-3}) plasma LPAs mainly because of the ubiquity of TW laser systems. In order to operate in the bubble regime, the laser pulse has to experience relativistic self-focusing in the plasma, and the critical power of relativistic self-focusing is $P_c = 1.7\omega_0^2/\omega_p^2$[GW], where ω_0 is the frequency of the laser, and ω_p is the plasma frequency. The typical plasma density for 1 TW laser to reach relativistic self-focusing is 2.6×10^{19} cm^{-3}. That is why many of the LPAs operate in high density plasma.

Moreover, high plasma density can induce stronger signal for plasma diagnostics. For instance, the Faraday rotation angle is proportional to the plasma density, and the phase shift in the spectral interferogram is also proportional to the density.

In this section, we will discuss the diagnostics that have been developed for LPAs in high density plasmas.

1.2.1 Faraday Rotation Diagnostic

Using Faraday effect to detect the magnetic field in plasma has been well-established. For instance, Stamper *et al.*[17] sent a probe beam through a target sample and put a polarizer in front of the detector. They imaged the probe beam on a film with different orientation of the polarizer. The intensity distribution revealed the magnetic field structure in the plasma. Walton *et al.* used a similar method to map the magnetic field at the ionization front of LPAs.

Kaluza *et al.* [18] extended the single detector approach to two detectors. In front of each detector there is a polarizer with a biased polarization angle. The polarizers were rotated to almost, but slight higher/lower than the minimum transmission. The biased angles were close to the expected rotation angle so that most of the beam was suppressed by the polarizer except for the region where the rotation occurred. Kaluza *et al.* used Faraday rotation diagnostic to obtain the magnetic field structure of the LPAs, which indicate the bubble structures. Flacco *et al.* [19] used similar technique to measure the

evolution of the magnetic field around the plasma bubble with multiple shots. The strong magnetic field around the plasma bubble ($\sim$ 100T) can persist for as long as 1.5 ps. Buck *et al.* [20] utilized the Faraday rotation diagnostic with an ultrashort probe pulse 8 fs to obtain the length of the accelerated electron bunch.

In these experiments, magnetic fields up to $\sim KT$, originating from the accelerated bunch and displacement currents within the evolving bubble, induced Faraday rotation preferentially in the bubble wall, where electron density n_e is about an order of magnitude higher than that of surrounding plasma. In all of these previous studies, however, the plasma density n_e exceeded 10^{19} cm^{-3}, limiting bubble size to $\lambda_p < 10$ μm and maximum accelerated electron energy to ~ 100 MeV due to dephasing and pump depletion limits. Moreover, the field of view of bubble propagation was limited to ~ 3 mm.

1.2.2 Frequency Domain Interferometry

As early as 1996, Sider *et al.* [21]obtained the time-resolved density oscillation of the laser induced plasma wakefield using spectral interferometry with multiple shots. The phase shift induced by the wakefield was extracted from the spectral interferogram of the reference and the probe pulse pair traversed the plasma wave.

In 2005, Matlis *et al.* [22] sent the reference and the probe pulse pair co-linearly with the driving pulse and obtained a snapshot of the wakefield in single shot, assuming that the plasma wave didn't evolve too much during the

interaction region. The snapshot revealed the dimension and the structure of the laser driven plasma wave for the first time.

Dong *et al.* [23] applied FDH to the LPAs in the nonlinear regime, the bubble regime, and showed that the bubble reshaped co-propagating chirped probe pulses into optical "bullets". Their result provided the first observation of bubble formation in single shot.

Li *et al.* extended the FDH technique to Frequency Domain Streak Camera (FDSC) by introducing an oblique angle between the pump and the probe beams[24], which allowed them to obtain a time-resolved evolution of the object. Li *et al.* applied FDSC to LPAs in the bubble regime and observed the evolution of bubble formation, propagation, and lengthening in a single shot[25].

1.2.3 Others

Thomas *et al.* measured the side scattering images of the LPAs and reported that the brilliant radiation in the beginning of the acceleration, the so-called wave-breaking radiation, was an indication of self-injection. Sávert *et al.* [26] used shadowgraphic technique to obtain snapshots of the plasma bubbles using a < 10 fs transverse probe. The shadwographic diagnostic revealed the evolution of the length of the plasma bubble in multiple shots. Their results showed that the plasma bubble lengthened before the occurrence of wave-breaking radiation, which means that the bubble expansion happened before self-injection. In other words, the shadowgraphic snapshot of the plasma

bubble indicated that the cause of bubble expansion is more like to be the intensity amplification of the driving pulse than the beam loading effect.

1.3 Diagnostics of GeV-Class LPAs

In order to accelerate the electrons to high energy, the laser pulse has to sustain the high intensity and self-guide for a long distance in the plasma. Moreover, the acceleration length is also limited by the size of the plasma bubble, which is roughly proportional to $1/\sqrt{n_e}$. Therefore, GeV-class LPAs require petawatt laser pulses to drive the plasma waves in low density (5×10^{17} cm^{-3}) plasmas. The scarcity of petawatt laser systems and the low plasma density make the diagnostics of GeV-class LPAs rare.

1.3.1 Multi-Object-Plane Diagnostic

In 2014, Li *et al.* have used Muti-object-plane technique to reveal the plasma bubble evolution of GeV-class LPAs in ~ 3 cm in single-shot[27]. A frequency doubled probe beam overlapped wth the LPA with a small angle and was split and imaged to four cameras, each one captured a different image plane. The phase shifts induced by the plasma wave were reconstructed by iteratively fitting the complete diffraction patterns in all cameras using a Gerchberg-Saxton algorithm. Nevertheless, the complex phase shift induced by the plasma channel around the bubble made extracting the signal extremely challenging.

1.3.2 Faraday Rotation Diagnostic

In 2016, we applied Faraday rotation diagnostic to GeV-class LPAs and obtained the plasma bubble structures. Larger bubble size enabled visualization of more subtle structural detail, and lengthened the propagation length over which probe polarization rotation accumulates, partially offsetting the effect of low density. Moreover, higher electron energy led to stronger magnetic fields than in previous work.

The rotation angle can be estimated by using

$$\phi_{rot} = \frac{e^3}{2c\epsilon_0 m_e^2 \omega^2} \int_\ell n_e \mathbf{B}_\varphi \cdot d\mathbf{s}, \tag{1.1}$$

where ω is the frequency of the probe beam, ℓ is the trajectory of the probe beam, n_e is the plasma density, $\mathbf{B}_\varphi$ is the azimuthal magnetic field , and $d\mathbf{s}$ is the path element along the path of the probe beam. Since n_e is almost zero inside the plasma bubble, ϕ_{rot} induced preferentially around the dense plasma bubble walls, on which the azimuthal magnetic induced by the accelerated electrons in relativistic regime scales as $\mathbf{B}_\varphi \propto N_{tot} \cdot \gamma / R_b^2 \propto N_{tot} \cdot E_{electron} \cdot n_e$, where N_{tot} is the total number of the accelerated electrons, γ is the Lorentz factor of the accelerated electrons, $E_{electron}$ is the energy of the accelerated electrons, and $R_b \propto \lambda_p \propto n_e^{-1/2}$ is the bubble radius. Therefore, form the expression of the rotation angle, we have $\phi_{rot} \propto N_{tot} \cdot E_{electron} \cdot n_e^{3/2}$. Although n_e in our experiment was almost 100 times lower than that in the previous experiments, N_{tot} and $E_{electron}$ were 100 and 20 times greater in our case. Eventually, the magnitude of the Faraday rotation angle in our experiment

was around the same order of the previous works.

We demonstrated that Faraday rotation signals are sensitive to transitions in the acceleration stages. Simulation [7] and analytical models [8] have previously suggested that the distribution of the dense plasma sheath around the bubble varies during the acceleration process. In the first stage of the acceleration where the driving pulse is self-focusing and the plasma bubble is expanding, the sheath electrons around the bubble experience long slippage time [28], gain the most energy, and therefore, are more likely to accumulate (to be trapped) on the back of the bubble [29]. Hence the plasma density on the back of the bubble is high in the first stage, and the return current of the plasma sheath can also induce strong azimuthal magnetic field on the back of the bubble [29]. In the second phase of the acceleration where the bubble stabilizes, the sheath electrons become less energetic and the population of the electrons on the back of the bubble is lower.

In 2017, we extended the one probe approach to multiple probe beams and obtained the evolution of the plasma bubble in single shot. We detected Faraday rotation signals on three probe beams, covering $\sim$ 3 cm interaction region. The data showed the transition of the plasma bubble from the first stage of the acceleration to the second stage.

1.4 Outlines of the dissertation

In this thesis, we will demonstrate the diagnostics we have developed for LPAs.

Chapter 2 is the manuscript that we plan to submit to Physics of Plasma. In this chapter, we demonstrate the that the Faraday rotation signals can reveal the plasma bubble structures of GeV-class LPAs. We also show that the Faraday rotation signals have different characteristics in different stages of the acceleration process. To verify our assessment, we performed a series of simulations using extended 2D (2D+1) Finite Difference Time Domain (FDTD) method.

In chapter 3, we present the experiment of Faraday rotation diagnostic of GeV-class LPAs with multiple probe beams. We generate probe beams in a compact beam sampler module and cover ~ 4 cm interaction region of the target. The Faraday rotation signals reveal the evolution of the plasma bubble within 3 cm range in single shot.

Chapter 4 is the manuscript that we plan to submit to Optics Letters. In this chapter, we demonstrated the upgraded version of FDSC, which can be used to reveal the dynamic of the plasma bubble in single shot. To resolve the bubble dynamics, one needs high temporal resolution, which requires a broad bandwidth probe beam. We expand the bandwidth of the probe beam using supercontinuum generation through a compact coverslip array, and demonstrate a prototype experiment to show that the broad bandwidth FDSC is capable of resolving the evolution of pulse self-steepening and temporal-splitting in glass in single shot.

Chapter 2

Faraday Rotation Diagnostics of The LPA - Single Probe

2.1 Introduction

[1] Since laser-plasma accelerators (LPAs) were first proposed in 1979 [1], LPAs have become a tabletop source of quasi-monoenergetic GeV electron bunches [2] and ultrafast X-ray pulses [3], for use in applications in biology, medicine, and materials science. The key to the compact size of LPAs is the unprecedented accelerating field (GeV/cm), contained in a light-speed, microscopic ($\sim 10^{-5}\ m$) plasma structure, in comparison to the conventional metal cavity ($\sim 1\ m$) radio-frequency accelerators. In particular, the highest-performing LPAs operate in a strongly nonlinear "bubble" or "blow-out" regime [6], where the driving laser pulse is intense enough to blow out electrons to form a plasma bubble.

Measuring the characteristics (e.g. size, shape, and bubble thickness) of plasma bubbles is essential to understanding the acceleration process of LPAs.

[1] This chapter is the manuscript that is going to be submitted to Physics of Plasma. The first author Y. Y. Chang is responsible for conducting the experiment, and the co-authors are: K. Weichman, X. Cheng, J. M. Shaw, J. Welch, M. LaBerge, A. Hannasch, R. Zgadzaj, A. Bernstein, W. Henderson, M. C. Downer

The bubble structures [4], [5],[6],[7] , [8] and the self-injection threshold have been studied analytically [7],[9], numerically[10], and experimentally [11],[12]. In addition, Kalmykov *et al.*[13] has suggested that the expansion rate of the plasma bubble has to exceed certain values to induce self-injection. Simulation [14] has also suggested that in a single-staged GeV-class LPA, the plasma bubbles can experience two phases in the acceleration process. In the first phase, when the driving pulse enters the plasma, the intensity of the pulse oscillates until the spot size matches the self-guiding conditions. During the intensity oscillations, the bubble expands when the driving pulse intensity decreases (due to defocusing), which leads to periodic self-injection[13]. In the second phase, the bubble structures stabilizes and the driving pulse starts to experience temporal compression [15] and etching effects [16]. The self-injection stops when the bubble stops expanding. The bubble structures and bubble dynamics of GeV-class LPAs, however, have not been experimentally characterized due to low plasma density ($\sim 5 \times 10^{17}\ cm^{-3}$) and long laser plasma interaction length ($\sim 10\ cm$).

Several previous experiments have visualized plasma bubble structures and dynamics in high density ($n_e \leq 10^{19}\ cm^{-3}$) plasmas. Dong *et al.* [23] showed that the bubble reshaped co-propagating chirped probe pulses into optical bullets, which in a single shot revealed bubble formation even below the threshold for relativistic electron production. However, Dong *et al.* did not observe dynamics or the internal structure of plasma bubbles. Li *et al.* [25] observed dynamics of bubble formation, propagation and lengthening in

a single shot by analyzing phase streaks imprinted on a chirped pulse propagating at a small angle to the bubble. Nevertheless, the thin bubble wall was not resolvable due to the limited probe bandwidth. Sávert *et al.* [26] obtained shadowgraphic snapshots of bubbles using a transverse probe with pulse length $\leq 10\ fs$, and observed changes in bubble structure over multiple shots. As for GeV-class LPAs operating in low density plasmas ($n_e = 5 \times 10^{17}$ cm^{-3}), Li *et al.* have used Muti-object-plane technique to reveal the plasma bubble evolution in $\sim 3\ cm$ in single-shot[27]. However, the complex phase shift induced by the plasma channel around the bubble made extracting the signal extremely challenging.

In addition, several investigators imaged Faraday rotation of a transverse probe pulse to measure the magnetic field inside [18] and outside [19] of the plasma bubbles, and to estimate the length of the accelerated electron bunch [20]. In all of these previous studies, however, the plasma density n_e exceeded 10^{19} cm^{-3}, limiting bubble size to $\lambda_p \leq 10\ \mu m$ and maximum accelerated electron energy to $\sim 100\ MeV$ due to dephasing and pump depletion limits. Moreover, the field of view of bubble propagation was limited to ~ 3 mm.

In our experiments, we extended Faraday rotation diagnostics for the first time to plasma density in the range $2 < n_e < 5 \times 10^{17}$ cm^{-3} — more than 20 times lower than in previous work — for which bubble size is of order $\lambda_p \sim 50\ \mu m$, and electron acceleration to multiple GeV is possible [14]. The rotation angle can be estimated by using

$$\phi_{rot} = \frac{e^3}{2c\epsilon_0 m_e^2 \omega^2} \int_\ell n_e \mathbf{B}_\varphi \cdot d\mathbf{s}, \tag{2.1}$$

where ω is the frequency of the probe beam, ℓ is the trajectory of the probe beam, n_e is the plasma density, $\mathbf{B}_\varphi$ is the azimuthal magnetic field , and $d\mathbf{s}$ is the path element along the path of the probe beam. Since n_e is almost zero inside the plasma bubble, ϕ_{rot} induced preferentially around the dense plasma bubble walls, on which the azimuthal magnetic induced by the accelerated electrons in relativistic regime scales as $\mathbf{B}_\varphi \propto N_{tot} \cdot \gamma / R_b^2 \propto N_{tot} \cdot E_{electron} \cdot n_e$, where N_{tot} is the total number of the accelerated electrons, γ is the Lorentz factor of the accelerated electrons, $E_{electron}$ is the energy of the accelerated electrons, and $R_b \propto \lambda_p \propto n_e^{-1/2}$ is the bubble radius. Therefore, form the expression of the rotation angle, we have $\phi_{rot} \propto N_{tot} \cdot E_{electron} \cdot n_e^{3/2}$. Although n_e in our experiment was almost 100 times lower than that in the previous experiments, N_{tot} and $E_{electron}$ were 100 and 20 times greater in our case. Eventually, the magnitude of the Faraday rotation angle in our experiment was around the same order of the previous works.

Furthermore, we demonstrated that Faraday rotation signals are sensitive to transitions in the acceleration phases. Simulation [7] and analytical models [8] have previously suggested that the distribution of the dense plasma sheath around the bubble varies during the acceleration process. In the first phase of the acceleration where the driving pulse is self-focusing and the plasma bubble is expanding, the sheath electrons around the bubble experience long slippage time [28], gain the most energy, and therefore, are more likely to ac-

cumulate (to be trapped) on the back of the bubble [29]. Hence the plasma density on the back of the bubble is high in the first phase, and the return current of the plasma sheath can also induce strong azimuthal magnetic field on the back of the bubble [29]. In the second phase of the acceleration where the bubble stabilizes, the sheath electrons become less energetic and the population of the electrons on the back of the bubble is lower.

In this paper, we will show that Faraday rotation signals have different characteristics in different phases of the acceleration process using extended 2D (2D+1) Finite Difference Time Domain (FDTD) simulations. In the first phase, since the plasma density and magnetic field are both high on the back of the bubble, the Faraday rotation signal is wide and the maximum is close to the center line (the laser axis). In the second phase, the plasma density of the back of the bubble decreases, but the density on the side sheath remains high. Thus, the Faraday rotation signal peaks at R_b (bubble radius) [16] above the center line. Since the peak of the experimental Faraday rotation signal is $\sim 25.4\ \mu m$ ($R_b \sim \sqrt{a_0}/k_p \sim 28.2\ \mu m$) above the laser axis, the plasma bubbles have reached the second phase of the acceleration when the bubble and probe beam overlapped.

In section II of this paper, we will present the experimental setup. In section III, we show the experimental results. In section IV, we demonstrate the relation between the Faraday rotation signals and the plasma bubble structures using FDTD simulations.

2.2 Experimental Procedure

Fig. 4.1 shows the schematic of the setup for measuring plasma bubble structures using Faraday rotation diagnostics at the Texas Petawatt Laser at the University of Texas at Austin.

A pump pulse with peak power 0.67 PW (100 J, 150 fs FWHM) at center wavelength 1.057 μm was focused at f/45 into a 1.5 mm radius entrance aperture of a 7 cm long gas cell filled with 5 Torr helium (He) with purity of 99.99%. The intense pump beam ionized the gas to generate plasmas ($n_{e0} \sim 2 \times 10^{17}\ cm^{-3}$), self-focused, generated nonlinear plasma waves (plasma bubbles), and accelerated electrons to high energy. A synchronized, linearly-polarized probe pulse propagated transversely through the side windows of the gas cell and overlapped with the plasma bubbles.

One challenge of applying Faraday rotation diagnostics to GeV LPAs was acquiring a wide horizontal field of view while maintaining a reasonable vertical resolution. According to PIC simulations, the plasma bubbles can propagate multiple centimeters, and the transverse diameter of the bubbles, which is critical to Faraday rotation signals, ranges from 40 μm to 60 μm. We used an anamorphic imaging system to demagnify the horizontal dimension to obtain wide field of view, but at the same time, magnify the vertical dimension to achieve a reasonable resolution.

The anamorphic imaging system consisted of three lenses (see Fig. 4.1(d)). Lens 1 was an objective lens with 15 cm focal length and 2" aperture

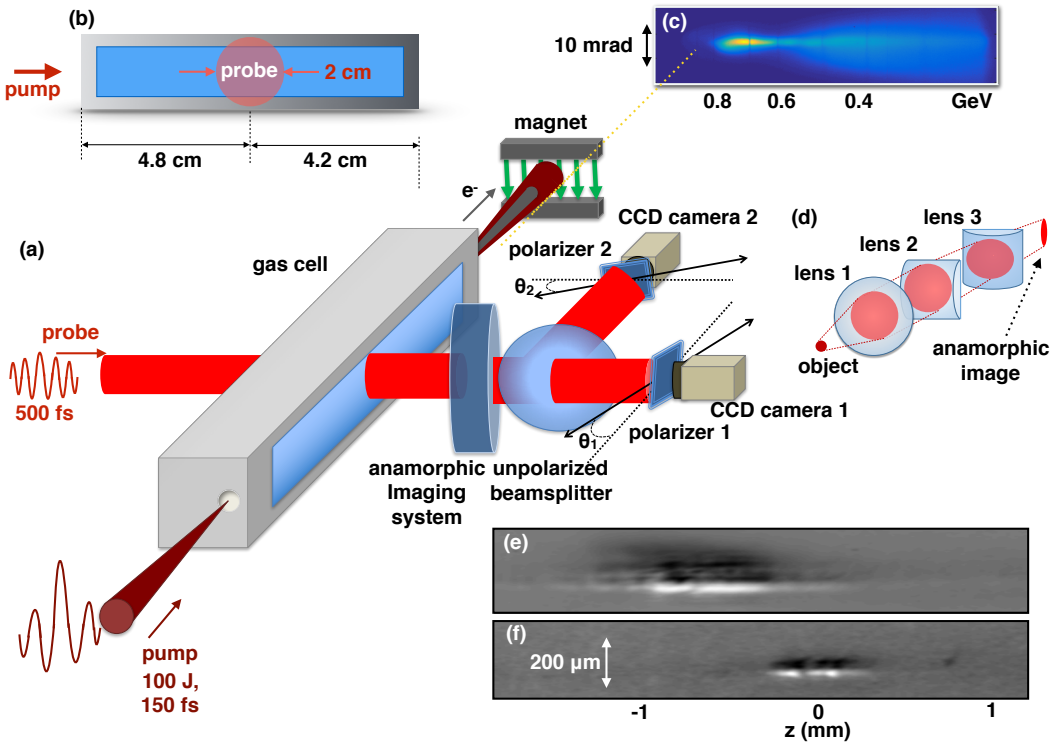

Figure 2.1: The schematic of the GeV LPA and the Faraday rotation diagnostics along with the signals from one particular shot. (a) The layout of the setup. (b) The side view of the gas cell. (c) The electron spectrum. (d) The layout of the anamorphic imaging system. Lens 1 is a spherical achromatic doublet with $f_1 = 15\ cm$. Lens 2 are both cylindrical achromatic doublets with $f_2 = 25\ cm$ and $f_3 = 5\ cm$. (e) and (f) The Faraday rotation angles of two consecutive shots with pump-probe delay changed $\sim 1.2\ ps$.

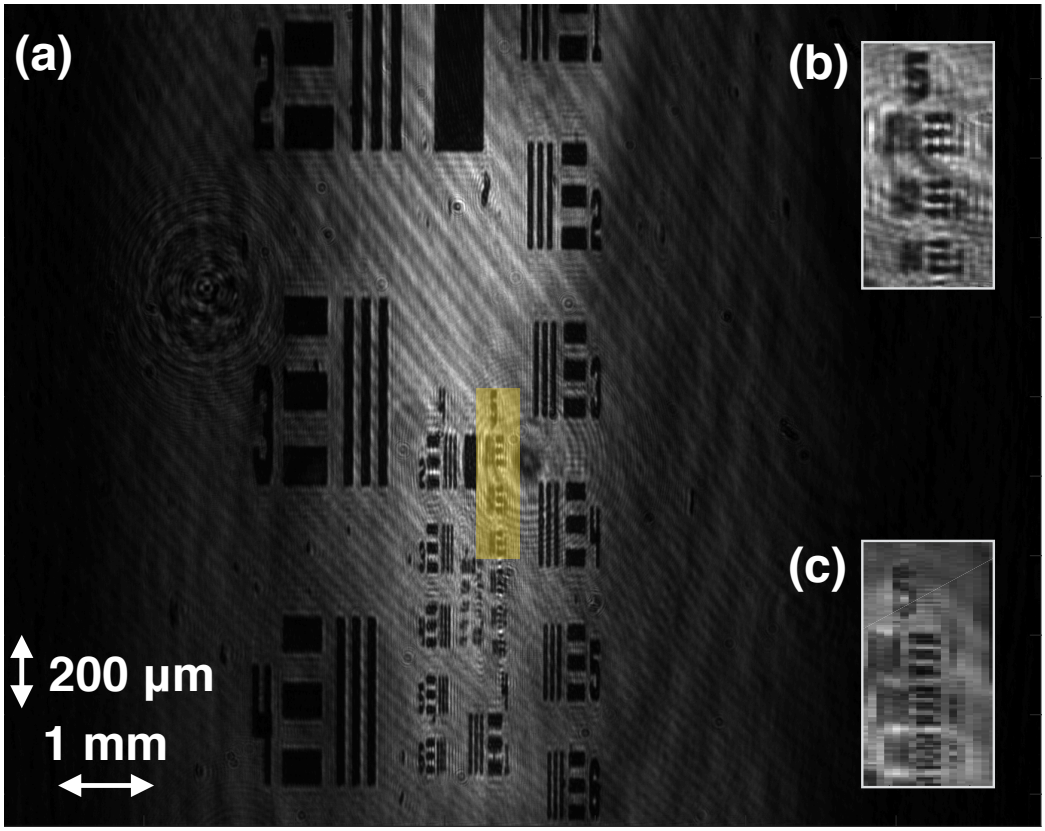

Figure 2.2: The images of a USAF resolution target through the anamorphic imaging system. (a): The full image. (b): zoom in of in-focused image. (c): zoom in of the image that is 400 μm away from the in-focused image plane.

to collect the light. Lens 2 was an 1" achromatic cylindrical lens with 25 cm focal length, and Lens 3 was an achromatic cylindrical lens with 5 cm focal length.The horizontal field of view of the imaging system was ~ 1.1 cm with ~ 50 μm resolution, and the vertical field of view was ~ 2.5 mm with ~ 12.5 μm resolution (see Fig. 3.2). The depth of field was up to 400 μm (Fig. 3.2 (c)).

To acquire a high signal-to-noise ratio in the rotation angle measurement, we split the probe beam with an unpolarized beamsplitter after the imaging system and sent the split beams to two cameras with polarizers in front of them as has been done by other researchers[18] ,[20]. The two polarizers in front of the cameras were rotated away from extinction in opposite directions with a small angle approximately equal to the expected rotation angle values ($\theta_i = \pm 2^\circ, i = 1, 2$). Since the two polarizers rotated with biased angles, the regions where the Faraday rotation occurred and the polarization was rotated clockwise was brighter on one camera and dimmer on the other. The same was true of the counterclockwise rotation. The measured intensity $\mathbf{I}_{pol,i}(y, z)$ can be described by Malus' law as

$$\mathbf{I}_{pol,i}(y, z) = \mathbf{I}_0(y, z) \cdot T_i \cdot (1 - \beta_i \cdot cos^2(\phi_{rot}(y, z) - \theta_i))$$

where ${}_0(y, z)$ is the intensity of the original probe beam, T_i is the transmission/reflection ratio of the beam splitter. $\beta_i (i = 1, 2)$ is the extinction ratio of the polarizers, where $(1 - \beta_1) = 6.1 \times 10^{-3}$ and $(1 - \beta_2) = 3.1 \times 10^{-3}$. The rotation angle can be extracted by dividing the intensity of the two images $\mathbf{I}_{pol,1}/\mathbf{I}_{pol,2}$. We matched the images of the two cameras according to the calibrated reference point.

2.3 Experimental Results

The Faraday rotation signals from the experiment are shown in Fig. 2.3, where the pump beam and the accelerated electrons propagate from left

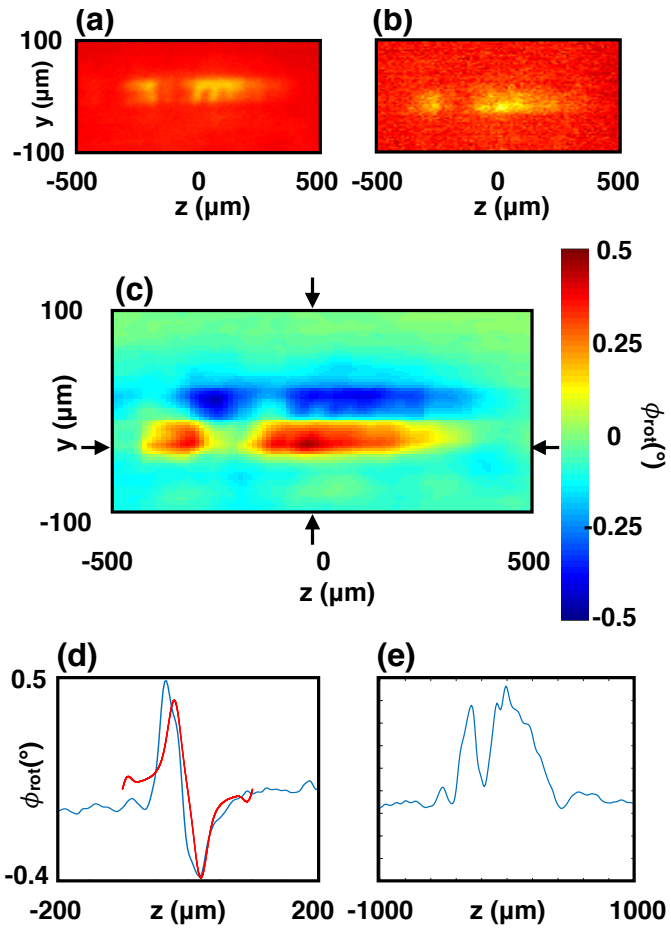

Figure 2.3: The Faraday rotation signals. (a) and (b) Raw images of camera 1 and 2. (c) The Faraday rotation signal converted from the raw images. (d) Blue line is the vertical lineout of the Faraday rotation signal, and red line is the result of the FDTD simulation. (see Fig. 3.7) (b) The horizontal lineout of the Faraday rotation signal.

to right. Note that the vertical and horizontal axes in the plots are not to scale because the probe beam was imaged through an anamorphic imaging system. The Faraday rotation signals were observed only in conjunction with accelerated electrons. Since the low plasma density results in the absence of plasma shadowing on the images, we were unable to precisely locate the relative position of the pump beam and the rotation angle signal. Therefore, we did several preliminary shots until we saw a definite Faraday rotation signal (Fig. 4.1(e)), and then we delayed the probe beam $\sim 1.2\ ps$ ($\sim 0.4\ mm$) in subsequent shots, and the signal shifted correspondingly (Fig. 4.1(f)). This iterative process for shifting the probe beam showed that the rotation angle signals were indeed sensitive to the overlapping of the pump and the probe beams.

The region where the Faraday effect is the strongest is symmetric around the laser axis (Fig. 2.3(c)). Since the Faraday effect is induced by the coupling of the magnetic field and plasma density, the magnitude of the rotation angle should be at its maximum around the region of the dense plasma around the bubble walls. Hence the distance between the peaks and valleys indicates the transverse size of the plasma bubble. The vertical lineout of the rotation angle signal agrees reasonably with the FDTD simulation (Fig. 2.3(d)), which shows that the Faraday rotation happened dominantly around the bubble walls .The average transverse distance between the peaks and the valleys of the rotation angle is $\simeq 50.8 \pm 10.1\ \mu m$, which matches the diameter of the plasma bubble ($R_p = \sqrt{a_0}/k_p \simeq 28.2\ \mu m$, where R_p is the radius of the

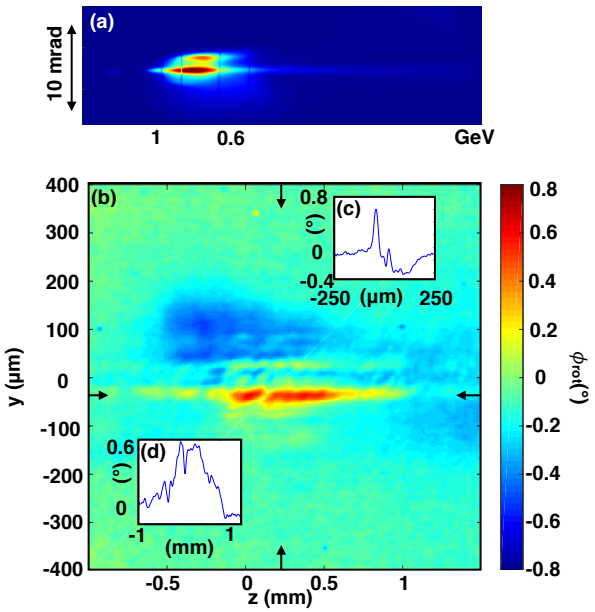

Figure 2.4: (a) The spectrum that shows two electron bunches. (b) The Faraday rotation signal of the same shot. (c) The vertical lineout of the Faraday rotation signal. (d) The horizontal lineout of the Faraday rotation signal.

plasma bubble, $a_0 \simeq 3.5$ is the normalized vector potential [2], and $k_p = 0.13$ μm^{-1}). The rotation signal indicated that the plasma bubble was fully blown out. The streak-like feature of the signal in this work was created by the long pulse length of the probe pulse ($\sim 500\ fs$).

Fig. 2.4(a) shows the electron spectrum for a shot in which accelerated electrons emerged in two bunches separated by $\sim$ 1 mrad in a direction perpendicular to the spectrometer's energy dispersion plane. We observe such bifurcation occasionally when the drive laser focuses to a doublepeaked intensity envelope, causing it to split into two filaments that drive parallel self-injected bubbles. The corresponding Faraday rotation signal (Fig. 2.4(b) shows broader structure in the bifurcation direction (y) than single-bubble shots (Fig. 2.3), indicative of the "doublebubble" structure of the interaction region.

In summary, our experimental results demonstrated that the Faraday rotation signals reveal the transverse diameter of plasma bubbles. We also showed that when we saw two electron bunches, we also saw more structures in the Faraday rotation signal.

2.4 FDTD Simulations and Discussion

In order to reveal the connection between the plasma bubble structures and the Faraday rotation signals, we performed a series of Finite difference time domain (FDTD) simulations. In the FDTD simulations, we sent a plane wave through static dielectric structures of the plasma bubble. The parameters

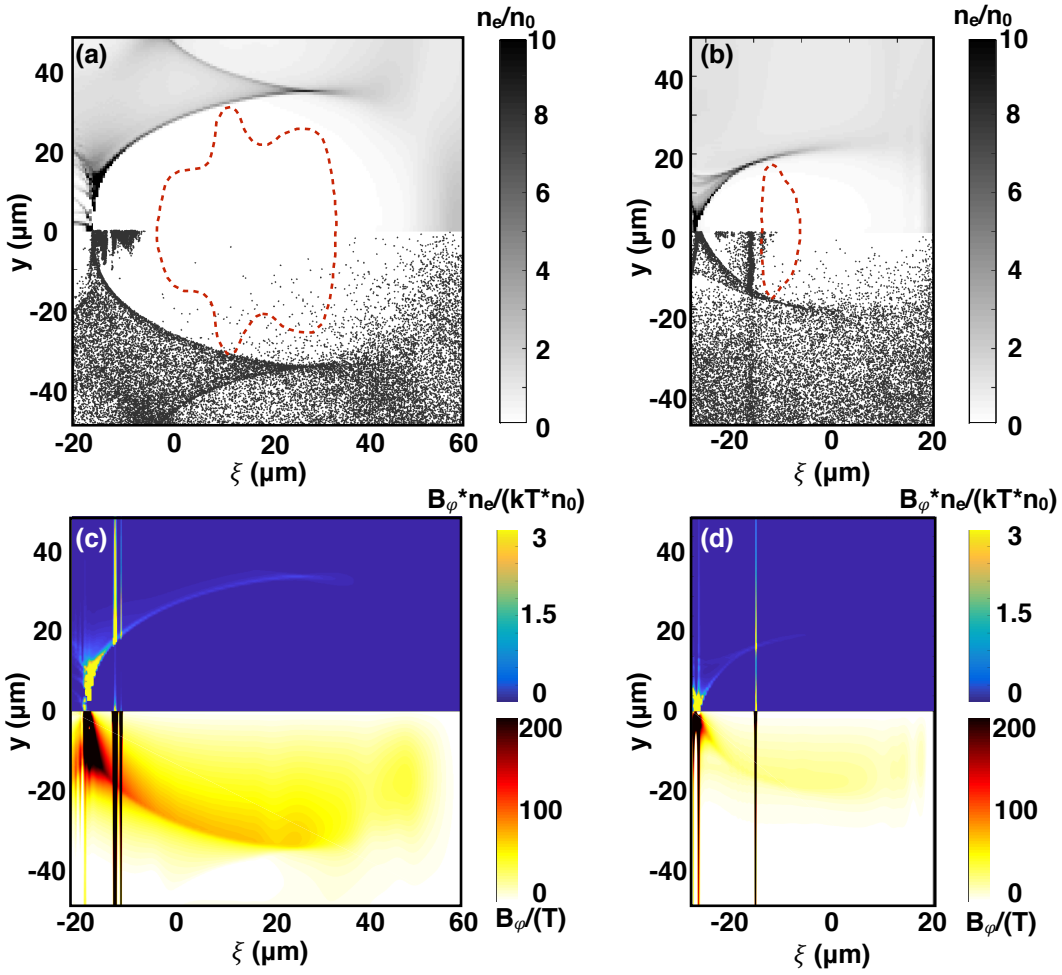

Figure 2.5: Simulation data from a cylindrically symmetric PIC code, WAKE. (a) and (b) plasma density (upper half) ($n_0 = 4.8 \times 10^{17}\ cm^{-3}$) and test particle distribution (lower half). The red dash lines are the contour lines of the driving pulse intensity. (c) and (d) $B_\varphi \cdot n_e$ (upper half) and B_φ (lower half) of the bubble. (a) and (c) Immediately after the self-injection happens. (b) and (d) 6 cm downstream after self-injection.

of the dielectric structures were taken from a cylindrically symmetric PIC wakefield simulation [2]·[14]. The PIC simulation was performed by using WAKE, a fully relativistic PIC code in axisymmetric geometry. (see Fig. 3.5)

Ideally, to obtain the Faraday rotation accurately, one needs to solve the eigenmodes and the dispersion relations of each grid and calculate the overall rotation (we call it ϕ_1) of the polarization of the probe beam after propagating through the magnetized plasma. However, solving eigenmodes and dispersion relation for each grid is time-consuming and not practical in simulations.

To simplify the problem, we considered only the $\mathbf{B}_\varphi \cdot \hat{\mathbf{k}}$ component of the magnetic field, where $\hat{\mathbf{k}}$ denotes the normalized wave vector of the probe beam (in our case, $\hat{\mathbf{k}} = \hat{\mathbf{x}}$), so the dielectric constant can be simplified as

$$\tilde{\epsilon}_r^{\pm} = 1 - \frac{\tilde{\omega}_p^2}{\tilde{\omega}(\tilde{\omega} \pm \tilde{\Omega}_B)}, \tag{2.2}$$

where $\tilde{\Omega}_B = e \cdot \tilde{B}_\varphi cos(\theta)/m_e$ is the cyclotron frequency, θ is the angle between $\tilde{\mathbf{B}}_\varphi$ and $\hat{\mathbf{k}}$, $\tilde{\omega}_p = \sqrt{\frac{\tilde{n}_e e^2}{\epsilon_0 m_e}}$ is the plasma frequency, $\tilde{\omega}$ is the frequency of the probe beam, and $\pm$ represents the right-handed and left-handed circularly polarized eigenmodes. The symbol $\sim$ denotes that the quantities are in the plasma rest frame. The rotation angle can now be written as

$$d\tilde{\phi}_2 = \frac{\tilde{\omega}}{c}\left(\sqrt{1 - \frac{\tilde{\omega}_p^2}{\tilde{\omega}(\tilde{\omega} - \tilde{\Omega}_B)}} - \sqrt{1 - \frac{\tilde{\omega}_p^2}{\tilde{\omega}(\tilde{\omega} + \tilde{\Omega}_B)}}\right)dx \tag{2.3}$$

Here, dx represents an infinitesimal step of the probe beam.

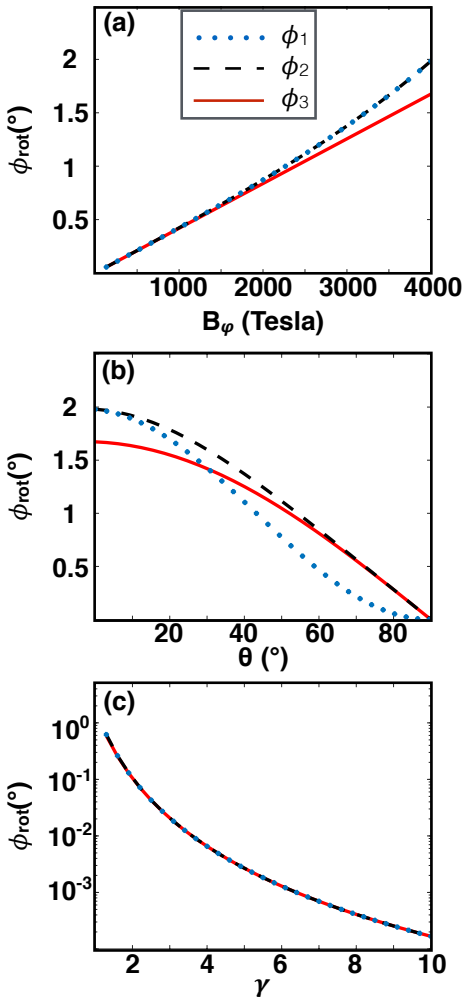

Figure 2.6: Faraday rotation angle calculated by different approaches. ϕ_1 is the obtained by finding the eigenmodes and solving the dispersion relations. ϕ_2 is calculated by Eq. (3.3), and ϕ_3 is calculated by Eq. (3.4). (a) ϕ_{rot} versus the magnitude of the magnetic field. $\theta = 0°$. The plasma thickness is $\Delta x = 50\ \mu m$. (b) ϕ_{rot} versus the angle between $\mathbf{B}_\varphi$ and $\hat{\mathbf{k}}$. $B_\varphi = 4000$ Tesla. $\Delta x = 50\ \mu m$. (c) ϕ_{rot} versus the Lorentz factor of the plasma flow. $\theta = 0°$, and $B_\varphi = 4000$ Tesla. $\Delta x = 50\ \mu m$.

Furthermore, when $\tilde{\Omega}_B \ll \tilde{\omega}$, Eq. (3.3) can be simplified as

$$d\tilde{\phi}_3 = \frac{\tilde{\omega}_p^2 \cdot \tilde{\Omega}_B}{2\tilde{\omega}^2 c} dx, \tag{2.4}$$

which ultimately leads to the expression of Eq. (3.1). The comparison of different methods of obtaining Faraday rotation angle (ϕ_1, ϕ_2, and ϕ_3) is shown in Fig. 3.6. Although ϕ_2 is not exactly the real value (ϕ_1), it is easier to calculate, and it slightly deviates from ϕ_1 only when θ is close to 90° where the rotation is already small. Therefore, in the following FDTD simulations, we will use Eq. (3.2) to calculate the dielectric constant. Since the data of the PIC simulation are in the lab frame, we are going to simply the problem and ignore the difference between the plasma rest frame and the lab frame, and we will discuss the difference afterwards.

In the first step, we performed two 2D FDTD simulations. We took a slice of the plasma bubble at the location of the accelerated electron bunch from the PIC simulation ($\xi = \xi_0 = -17\ \mu m$ in Fig. 3.5 (a) and (c)) , calculated the dielectric distribution of the bubble slice, namely, $\epsilon_r^{\pm}(x, y, \xi = \xi_0) = 1 - \frac{\omega_p(x,y,\xi=\xi_0)^2}{\omega(\omega \pm \Omega_B(x,y,\xi=\xi_0))}$, and sent a plane wave through the dielectric structure. The plane wave propagated along x-axis and was linearly polarized in y-axis. The wavelength of the plane wave was 1.054 μm, the same as the probe beam in the experiment.

In order to reveal the connection between the Faraday rotation signal to the thickness of the bubble walls, we varied the thickness of the plasma

density outside of the bubble while kept the total particle numbers conserved. The FWHM of the bubble densities were 1.64 and 8.23 μm, and the peaks of the densities were 7.4 and 1.48×10^{18} cm^{-3} respectively.

Fig. 3.7 shows the results of the 2D FDTD simulations. The plane wave propagates from left to right, and the polarization of the beam is along the y-axis. The color scale shows the polarization rotation of the probe beam (Fig. 3.7 (a) and (b)), and the lineout plots (Fig. 3.7 (c) and (d)) show the rotation angle signals imaged by a nearly perfect ($f/0.08$) imaging system.

In Fig. 3.7(c) and (d), we chose two different object planes, one at the center of the bubble (in-focus, blue line) and the other one 30 μm downstream (out-of-focus, red line). The out-of-focused rotation angle signal was diffracted (Fig. 3.7 (d) red lines) when the thickness of the bubble wall was close to the wavelength of the probe beam.

In both cases, the distance between peak and valley of the rotation angles matches the diameter of the plasma bubble, which proves that Faraday rotation occurs preferentially on the bubble walls. The theoretical estimation of the maximum value of the rotation angle was $\sim 1^{\circ}$, which agrees with the simulation results.

To interpret the experimental results further, we extended the 2D simulation and performed two 2D+1 FDTD simulations . This time, we calculated the dielectric distribution of the bubble as $\epsilon_r^{\pm}(x, y, \xi) = \sum_i \epsilon_r^{\pm}(x = x_i + \xi, y, \xi)$, and sent a plane wave along $x = \xi$ axis, which means that the plane wave

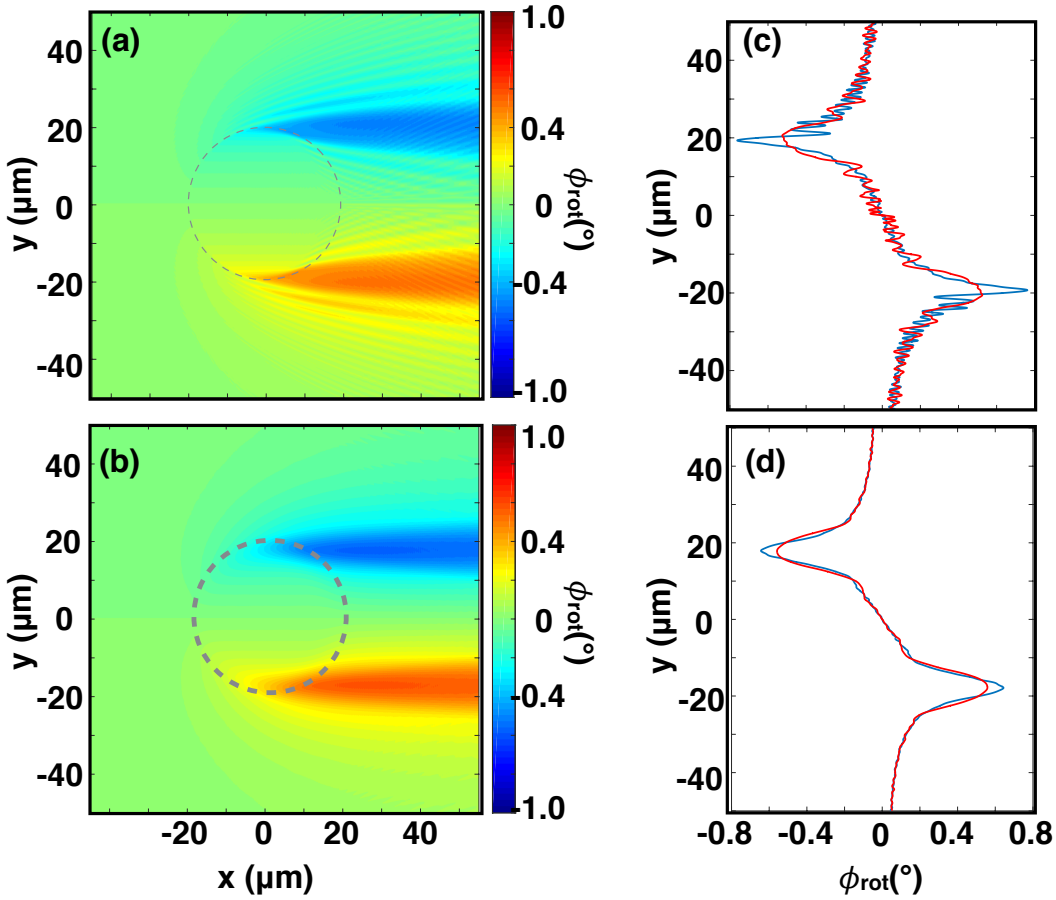

Figure 2.7: (a) and (b) 2D FDTD Simulation of the Faraday rotation induced by the plasma bubbles. The thickness of the the bubble walls are 1.64 and 8.23 μm respectively. (c) and (d) Lineouts of the simulated rotation angle signals imaged by a near perfect imaging system (f/0.08). The object planes are on the center of the plasma bubble (in-focus, blue lines) and 30 μm downstream (out-of-focus, red lines).

overlapped with the bubble with 45°, as how the probe beam actually overlapped with the bubble in the experiment. Here, $\{x_i\}$ are the pixels on the x axis from the PIC simulation. Similar to the 2D simulation, the probe beam was linearly polarized in y-axis. The difference here is that, instead of using a thin plane wave, we added a pulse length to the probe beam where $\tau_L = 100$ fs.

We took two different bubble parameters from the PIC simulation. The first bubble parameter was immediately after the self-injection happened where the bubble was expanding (Fig. 3.5 (a)). This was in the first phase of the acceleration process. The other bubble structure was 6 cm downstream after self-injection happened where the bubble stabilized (Fig. 3.5(b)). This was in the second phase of the acceleration process.

In the first phase of the acceleration when the bubble is expanding, large amounts of electrons, both passing electrons and injection candidates, aggregate on the back of the bubble ($n_e \sim 1 \times 10^{19}$ cm^{-3}) . Moreover, about 98% of the electrons have forward momentum $P_z/(m_e c) > 10$ because they experience long slippage time around the bubble[28]. Therefore, the electrons on the back of the bubble induce a strong azimuthal magnetic field (> 500 T) (Fig. 3.5(c), bottom half). As a result, the injected electrons contribute little to $B_\varphi \cdot n_e$ (Fig. 3.5(c), top half) even though the magnetic field induced by them is > 300 T on the bubble wall. In the second phase of the acceleration, however, the electron aggregation on the back of the bubble reduces, and the azimuthal magnetic field is less intense on the back of the bubble (Fig. 3.5

(d), bottom half). Subsequently, the contribution of the accelerated electron bunch to $B_\varphi \cdot n_e$ is more significant (see Fig. 3.5(d), top half).

Fig. 3.8 shows the Faraday rotation signals of the probe beam after propagating through the bubble. In the first phase of the acceleration, the peak of the rotation angle signal (Fig. 3.8(a)) is close to the center ($\sim 9.4\ \mu m$ above the laser axis) because the $B_\varphi \cdot n_e$ is high on the back of the bubble. In addition, the rotation angle signal spreads almost 30 μm above the center because of the large size of the bubble. The big volume of the bubble also increases the interaction length, which enhances the magnitude of the rotation angle. In the second phase, the maximum of the rotation angle locates at $\sim 17.4\ \mu m$ above the center (Fig. 3.8 (b)), while the intense region of $B_\varphi \cdot n_e$ induced by the accelerated electron bunch is 16.58 μm above center (Fig. 3.5(d), upper half), which shows that the contribution of the electron bunch is more relevant in the second phase. Therefore, in the second phase, due of the reduction of $B_\varphi \cdot n_e$ on the back of the bubble, the location of the maximum of the rotation angle can better represent the size of the bubble.

By comparison, the Faraday rotation signal from the second phase is more similar to the experimental data in terms of the magnitude and the location of the maximum, which indicates that the bubble has fully blown out and reached the second phase of the acceleration process when it overlapped with the probe beam. However, the experimental results didn't show any significant peak close to the laser axis, while the simulation shows a secondary peak near the center in the second phase. The discrepancy of the experiment

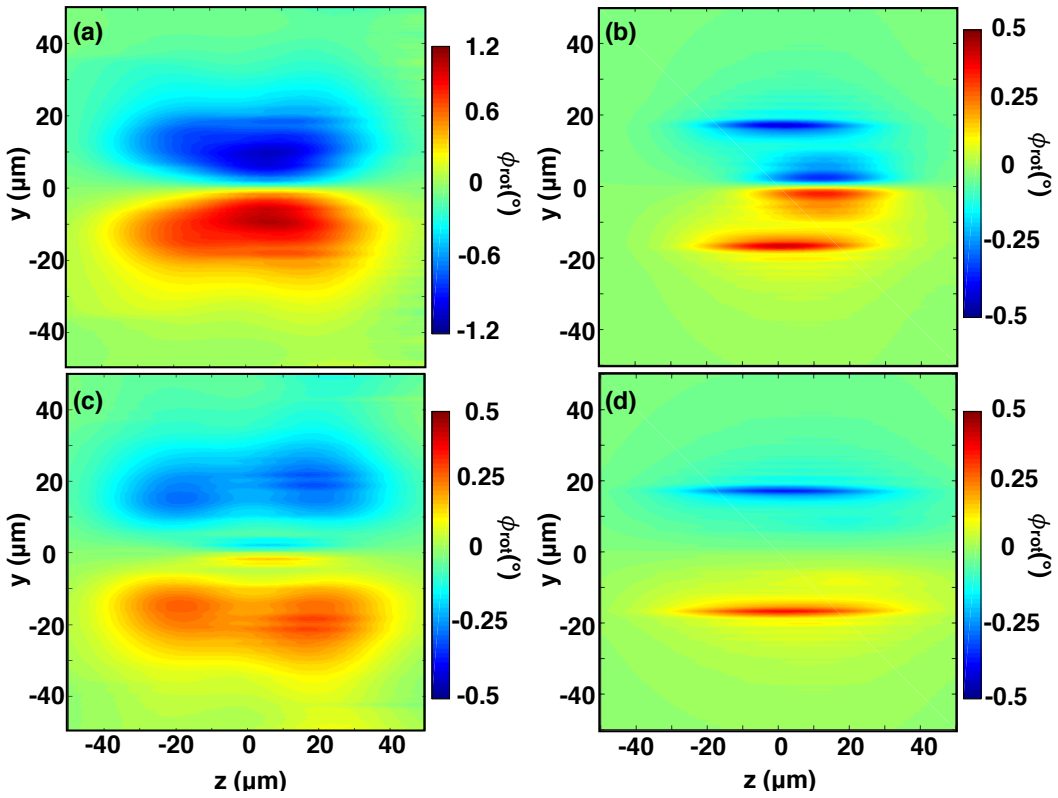

Figure 2.8: Faraday rotation signals from 2D+1 FDTD simulation. (a) The rotation angle of the probe beam after propagating through the bubble in the first phase of the acceleration. (b) The rotation angle of the probe beam after propagating through the bubble in the second phase of the acceleration. (c) The rotation angle of the first phase after considering the relativistic effect. (d) The rotation angle of the second phase after considering the relativistic effect.

and simulation can be explained by considering the relativistic plasma flow of the bubble.

So far in the FDTD simulations, we assumed that the plasma bubble was static. We used the data from the PIC simulation, which were in the lab frame, to calculate the dielectric constant ϵ_r. However, in reality, part of the plasma bubble (especially the back of the bubble) flew relativistically along with the driving beam. Therefore, we need to include the relativistic effect to calculate the dielectric constant in the plasma rest frame.

To calculate the dielectric constant in Eq. (3.2), we need to convert three quantities from the lab frame to the rest frame of plasma [30]. The first one is the plasma density, $\tilde{n}_e = n_e/\gamma$. The second one is frequency of the probe beam, $\tilde{\omega} = \gamma(1 - \beta \cdot \hat{\mathbf{k}})\omega$, and the third one is the magnetic field, $\tilde{\mathbf{B}}_\varphi = (\mathbf{1} + \gamma^2\beta\beta) \cdot \mathbf{B}_\varphi/\gamma$. Here γ is the Lorentz factor and β is the velocity of the plasma flow. After considering the relativistic effect of the plasma flow, the rotation angle ϕ_{rot} is proportional to $1/\gamma^4$ as shown in Fig. 3.6(c).

The result of FDTD simulation with the relativistic effect of the plasma flow is shown in Fig. 3.8(c) and (d). In Fig. 3.8(c), the magnitude of the rotation angle decreases drastically due to the relativistic effect. In particular, the rotation angle close to the laser axis is suppressed the most. Nevertheless, there is a residual peak at $y \simeq 2\ \mu m$, and the shape of the rotation angle is still wide. On the other hand, the data in Fig. 3.8(d) shows almost no rotation in the region close to the laser axis, while the amount of the rotation away from the laser axis is nearly unchanged. The reason can be explained as follows.

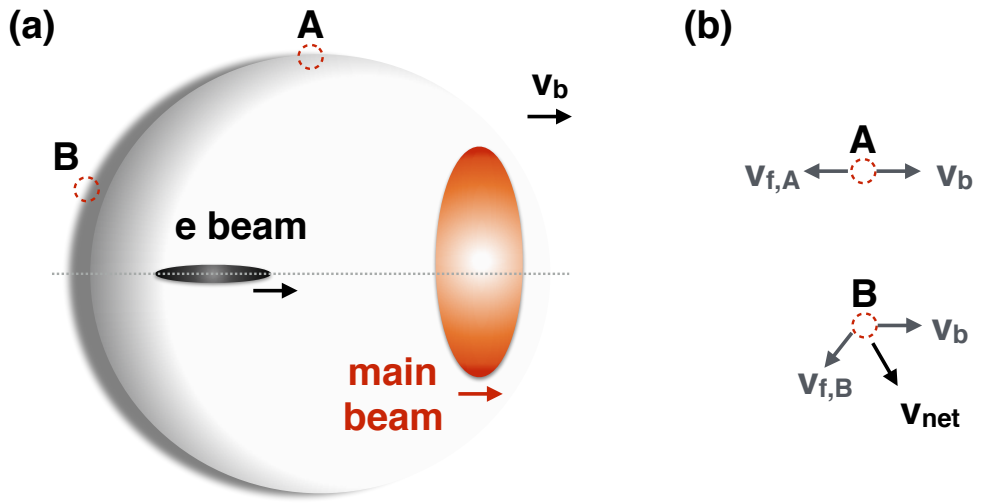

Figure 2.9: Diagram of plasma bubble and the plasma flow. (a) plasma bubble induced by a laser pulse. (b) qualitative explanation of the plasma net flow at different positions of the bubble wall in the lab frame.

Suppose that the bubble propagates through the plasma with velocity v_b (see Fig. 3.9). Electrons in the bubble wall flow around its periphery with velocity v_f in the bubble's rest frame. In a non-relativistic calculation for a "stable" bubble (Fig. 3.8(b)), streaming electrons at the side wall (position A on Fig. 3.9(a)) of the bubble contribute the outer Faraday shift lobe ($\sim 20\ \mu m$ from axis), whereas streaming electrons at position B of Fig. 3.9(a) near the back of the bubble (5 to 10 μm from axis) contribute the inner lobe, which is not observed in the experiments. In the lab frame (where the measurement is made), electrons at the side wall have velocity $v_b - v_{f,A} \sim 0$ (see Fig. 3.9(b)), whereas electrons at the back of the bubble have velocity $v_{net} \sim 0.97c$ (gamma ~ 4) given by the vector sum of v_b and $v_{f,B}$. Consequently the Faraday rotation from these electrons is suppressed by a factor $1/\gamma^4 \sim 1/256$ (or more). This explains the relative weakness of the shift near the propagation axis.

To summarize, the FDTD simulation showed that the Faraday rotation signals have different shapes and distributions when the bubble structures changes, especially in the two phases of acceleration. These simulation results indicated that, in the experiment, the plasma bubbles have entered the second phase of the acceleration process when it overlapped with the probe beam, which was $\sim 50\%$ of the full laser-plasma interaction region. Furthermore, the relativistic effect of the plasma bubble flow can influence the magnitude and the shape of the rotation angle.

2.5 Conclusion

In conclusion, we were able to measure the transverse diameter of plasma bubbles of GeV LPAs using Faraday rotation diagnostics. The experimental results showed that the bubble has entered the second phase of the acceleration process after $\sim 50\%$ of full laser-plasma interaction region. The FDTD simulations suggested that the Faraday rotation signals are sensitive to the plasma bubble structures.

Chapter 3

Single-shot movies of evolving GeV laser-plasma accelerators by multiplexed Faraday rotation

3.1 Introduction

[1]

Since laser-plasma accelerators (LPAs) were first proposed in 1979 [1], LPAs have become a tabletop source of quasi-monoenergetic GeV electron bunches [2] and ultrafast X-ray pulses [3], for use in applications in biology, medicine, and materials science. The key to the compact size of LPAs is the unprecedented accelerating field (GeV/cm), contained in a light-speed, microscopic ($\sim 10^{-5}$ m) plasma structure, in comparison to the conventional metal cavity (~ 1 m) radio-frequency accelerators. In particular, the highest-performing LPAs operate in a strongly nonlinear "bubble" or "blow-out" regime [6],[4],[5],[7], [8], where the driving laser pulse is intense enough to blow out electrons to form a plasma bubble.

[1] Y.-Y.C. conducted the Faraday rotation multiplexing diagnostic and analysis, K.W. and X.C. performed the relativistic effect analysis. X.C. provided the PIC simulation data. J.M.S. and M.L. performed the electron spectrum analysis, J.W. performed the electron simulations, R.Z. designed the Faraday rotation multiplexing setup, W.H. designed and built the gas cell, and A.B. and M.C.D. are the executive of the experiments. All authors reviewed the manuscript. The work is under the reviewing process with Nature Communications.

Studies[2],[16],[14] have shown that petawatt class pulses are capable of generating multi GeV electrons in low density plasmas (a few 10^{17} cm^{-3}) in a single-stage setup. Due to the restriction of the dephasing length of LPAs[31], low density plasma is required to generate multi GeV electrons. Petawatt class pulse is necessary because the drive pulse needs to be overcritical to achieve relativistic self-focusing (RSF) [32], which allows a pulse to propagate over multiple Rayleigh length in underdense plasma, with[33] or without[2] a pre-formed waveguide. Moreover, self-injection[7],[9],[10],[11],[12], where the laser induced ion cavity, the plasma bubble, attracts and accelerates the ambient plasma electrons, is essential for single-stage LPAs.

A few injection methods of LPAs have been proposed[34]. Especially, Kalmykov *et al.* [14] have suggested using mismatched focus geometry to introduce self-injection for single-stage, GeV-class LPAs. The spot size of self-guided pulse is matched as $R_{sg} \approx 2.3(P/P_{cr})^{1/6}/k_p$ according to simulation[14], where $P_{cr} = 16.2(\omega_0/\omega_p)^2$ GW is the critical power[32] of RSF, ω_0 is the laser frequency, ω_p is the plasma frequency, and $k_p = \omega_p/c$. However, when the initial spot size (R_L) of the drive pulse is few times higher than R_{sg}, the pulse experiences intensity oscillations in the early stage of the propagation, which leads to plasma bubble expansion and contraction. The changing of the bubble size then induces periodic electron self-injection[13]. Later on in the acceleration process, the bubble becomes stable and the drive pulse starts to experience temporal compression [15] and etching effects [16]. The self-injection stops when the bubble ceases expanding. Although the transition

from oscillation to stabilization of the bubble has been demonstrated in simulations, the bubble structures and dynamics of GeV-class LPAs, however, have not been experimentally characterized due to low plasma density ($\sim 5 \times 10^{17}$ cm^{-3}) and long laser plasma interaction length (~ 10 cm).

Several previous experiments have visualized plasma bubble structures and dynamics in high density ($n_e \leq 10^{19}$ cm^{-3}) plasmas. Dong *et al.* [23] showed that the bubble reshaped co-propagating chirped probe pulses into optical "bullets," which in a single shot revealed bubble formation even below the threshold for relativistic electron production. However, Dong *et al.* did not observe dynamics or the internal structure of plasma bubbles. Li *et al.* [25] observed dynamics of bubble formation, propagation and lengthening in a single shot by analyzing phase streaks imprinted on a chirped pulse propagating at a small angle to the bubble. Nevertheless, the thin bubble wall was not resolvable due to the limited probe bandwidth. Sávert *et al.* [26] obtained shadowgraphic snapshots of bubbles using a transverse probe with pulse length ≤ 10 fs, and observed changes in bubble structure over multiple shots. However, their LPAs operated in high density plasma ($n_e > 10^{19}$ cm^{-3}) and the evolution of the bubble was obtained through multiple shots.

As for GeV-class LPAs operating in low density plasmas ($n_e = 5 \times 10^{17}$ cm^{-3}), Li *et al.* have used Muti-object-plane technique to reveal the plasma bubble evolution in ~ 3 cm in a single shot[27]. However, the complex phase shift induced by the plasma channel around the bubble made extracting the signal extremely challenging. In addition, Zhang *et al.* [35] have utilized high

energy electron bunches generated by LPAs to probe the structures of laser induced plasma waves in density as low as 3×10^{17} cm^{-3}. Nevertheless, the detected plasma wave was in the linear regime, not in the bubble regime.

Furthermore, several investigators utilized Faraday rotation of a transverse probe pulse to measure the magnetic field inside [18] and outside [36],[19] of the plasma bubbles, and to estimate the length of the accelerated electron bunch [20]. In all of these studies, however, the plasma density n_e exceeded 10^{19} cm^{-3}, limiting bubble size to $\lambda_p \leq 10$ μ m and maximum accelerated electron energy to ~ 100 MeV due to dephasing and pump depletion limits. Moreover, the field of view of bubble propagation was limited to ~ 3 mm.

Here we present the movies of evolving plasma bubble of GeV-class LPAs using Faraday rotation multiplexing diagnostic in a single shot. In our experiments, we extended Faraday rotation diagnostics to plasma density in the range $2 < n_e < 5 \times 10^{17}$ cm^{-3} - over 20 times lower than that in the previous works - for which bubble size is of order $\lambda_p \sim 50$ μm, and electron acceleration to multiple GeV is possible [14]. The rotation angle can be estimated by using

$$\phi_{rot} = \frac{e^3 \lambda^2}{8\pi^2 c^2 \epsilon_0 m_e^2} \int_\ell n_e \mathbf{B}_\varphi \cdot d\mathbf{s}, \tag{3.1}$$

where λ is the wavelength of the probe beam, ℓ is the trajectory of the object, n_e is the plasma density, $\mathbf{B}_\varphi$ is the azimuthal magnetic field , and $d\mathbf{s}$ is the path element along the path of the probe beam. Since n_e is almost zero inside the plasma bubble, ϕ_{rot} induced preferentially around the dense plasma bubble

walls, on which the azimuthal magnetic induced by the accelerated electrons in relativistic regime scales as $\mathbf{B}_\varphi \propto N_{tot} \cdot \gamma / R_b^2 \propto N_{tot} \cdot E_{electron} \cdot n_e$, where N_{tot} is the total number of the accelerated electrons, γ is the Lorentz factor of the accelerated electrons, $E_{electron}$ is the energy of the accelerated electrons, and $R_b \propto \lambda_p \propto n_e^{-1/2}$ is the bubble radius. Considering the integration path length is proportional to the bubble radius, we have $\phi_{rot} \propto N_{tot} \cdot E_{electron} \cdot n_e^{3/2}$. Although n_e in our experiment was ~ 40 times lower than that in the previous experiments, N_{tot} and $E_{electron}$ were around 30 and 10 times greater in our case. Eventually, the magnitude of the Faraday rotation angle in our experiment was around the same order of magnitude of the previous works.

Furthermore, we demonstrate that Faraday rotation signals are sensitive to transitions in the acceleration stages using multiple probe pulses in a single shot. Simulation [7] and analytical models [8] have previously suggested that the distribution of the dense plasma sheath around the bubble varies during the acceleration process. When the bubble is just formed and the driving pulse is self-focusing, the sheath electrons around the bubble experience long slippage time (surf on the wake) [28], gain the most energy, and therefore, are more likely to accumulate (to be trapped) on the back of the bubble [29]. Hence the plasma density on the back is high when the bubble is just formed, and the plasma sheath can also induce strong azimuthal magnetic field on the back of the bubble [29]. Afterwards when the bubble stabilizes, the sheath electrons become less energetic and the population of the electrons on the back of the bubble is lower. We have performed a series of simulations using finite

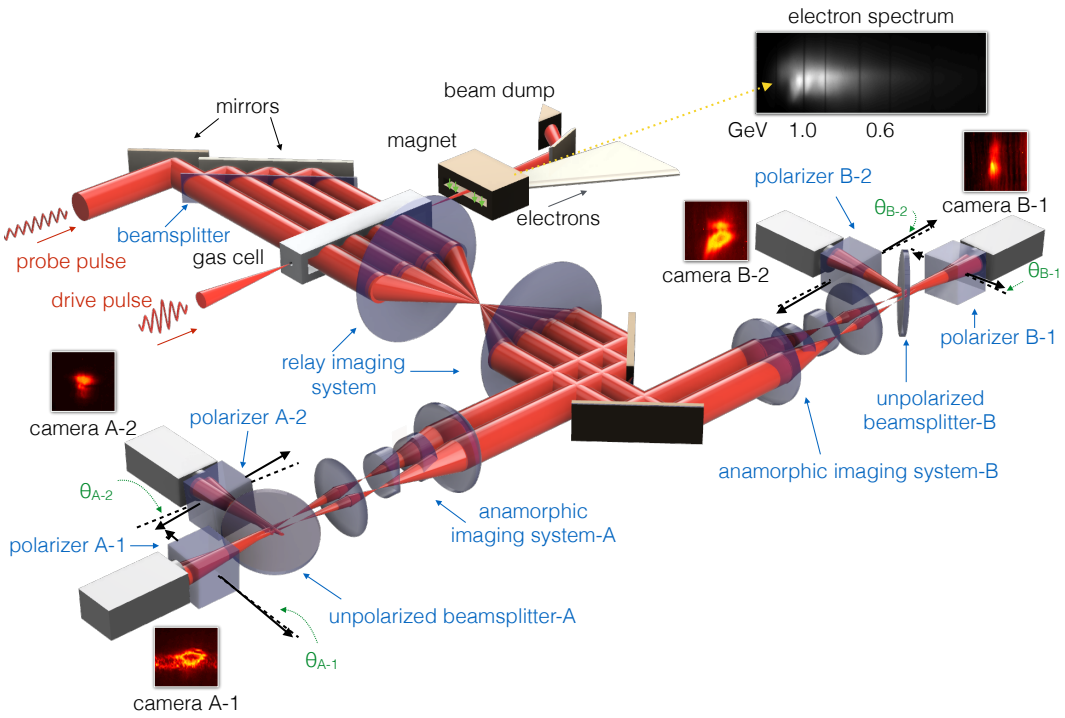

Figure 3.1: **Experimental setup**. The schematic of the GeV LPA and the Faraday rotation multiplexing diagnostic. The anamorphic imaging system is composed of one spherical achromat doublet and two cylindrical lenses. The focal length of the spherical achromat is 15 cm, and the focal length of the cylindrical lenses are 25 cm and 5 cm respectively.

different time domain method (FDTD) to explain the experimental results.

3.2 Results

3.2.1 Faraday rotation signal of stabilized bubble

Fig. 4.1 shows the schematic of the setup for obtaining plasma bubble evolution using Faraday rotation multiplexing at the Texas Petawatt Laser at the University of Texas at Austin.

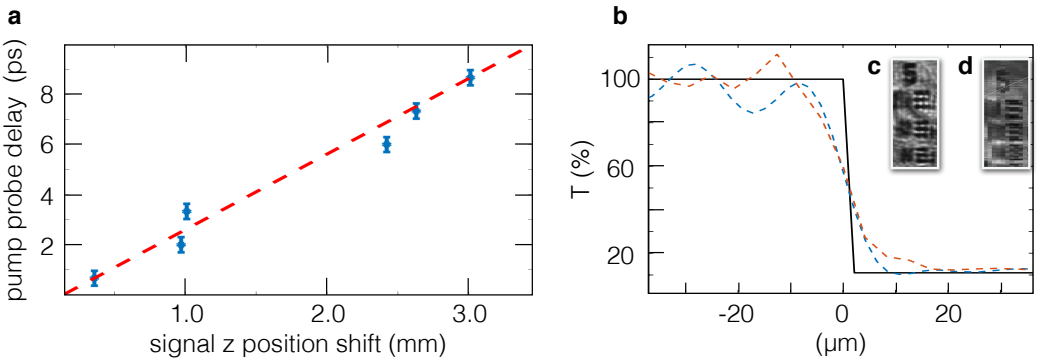

Figure 3.2: **The pump probe delay scan and the resolution of the anamorphic imaging system.** (**a**), The displacement of the Faraday rotation signals versus the changes of the pump-probe delay. The error bar is based on the timing jitter of the probe pulses ($\pm$133 fs) (**b**), The averaged vertical lineout of group 4 element 2. Black solid line is the object. The blue dash line is the lineout when the image is in focus, and the red dash line is the lineout when the image is 300 μm out of focus. The vertical axis is the normalized transmission in percentage. **c**, Zoom in of the anamorphic image. The vertical resolution is around 8.8 μm. **d**, Zoom in of the image that is 300 μm away from the in-focused image plane.

A drive pulse with peak power 0.67 PW (100 J, 150 fs FWHM) at center wavelength 1.057 μm was focused at f/40 (focal spot size FWHM is $R_L \approx 80$ μm) into a 1.5 mm radius entrance aperture of a 7 cm long gas cell filled with 5 Torr helium (He) with purity of 99.99%. The intense drive pulse ionized the gas to generate plasmas ($n_{e0} \approx 5 \times 10^{17}$ cm^{-3}), self-focused, generated nonlinear plasma waves (plasma bubbles), and accelerated electrons to high energy. The details of the laser system and the gas cell design can be found in Wang *et al.*'s report[2].

To begin with the simple case, we sent one synchronized transverse probe pulse, with pulse length $\sim$ 2 ps and diameter $\sim$ 2 cm, to obtain the Faraday rotation signal in the region where the plasma bubble was expected to be stabilized. The long pulse length and the wide pulse size with respect to the bubble size were chosen so that the probe pulse could overlap with the plasma bubble more easily. The center of the probe pulse was 38 mm away from the entrance of the gas cell, which is around the region where the plasma bubble should be stabilized according to the simulation [14]. As for the polarimetry technique, we followed the procedures that have been demonstrated previously by other research groups [18],[20] (see Methods 3.4.1). To acquire a high signal-to-noise ratio in the rotation angle measurement, we split the probe beam with an unpolarized beamsplitter after the imaging system and sent the split beams to two cameras with polarizers in front of them as has been done by other researchers25 ,27. The two polarizers in front of the cameras were rotated away from extinction in opposite directions($\theta_{A-1} = -2°$, $\theta_{A-2} = 2°$,

$\theta_{B-1} = -2.1°$, and $\theta_{B-2} = 2.1°$). Since the two polarizers rotated with biased angles, the regions where the Faraday rotation occurred and the polarization was rotated clockwise was brighter on one camera and dimmer on the other. The same was true of the counterclockwise rotation.

The probe was linearly polarized to the same polarization of the drive pulse so that most of the background was suppressed by the polarizers in front of the detectors. Since the low plasma density does not produce significant of plasma shadowing on the images, we were unable to precisely locate the relative position of the pump beam and the rotation angle signal. Therefore, we did several preliminary shots until we saw a definite Faraday rotation signal, and then we delayed the probe pulse in subsequent shots, and the signal shifted correspondingly (Fig. 3.2a). This iterative process for shifting the probe pulse delay showed that the rotation angle signals were indeed sensitive to the overlapping of the pump and the probe pulses.

One challenge of applying Faraday rotation diagnostics to GeV LPAs is acquiring a wide horizontal field of view while maintaining a reasonable vertical resolution. According to simulations[14], [16] , the plasma bubbles can propagate multiple centimeters, and the transverse diameter of the bubbles, which is critical to Faraday rotation signals, ranges from 40 to 60 μm. Therefore, we used an anamorphic imaging system to demagnify the horizontal dimension to obtain wide field of view (29.4 mm), but at the same time, magnify the vertical dimension to achieve a reasonable resolution (8.77 μm) with depth of field ~ 300 μm (Fig. 3.2c and d). The details of the anamorphic

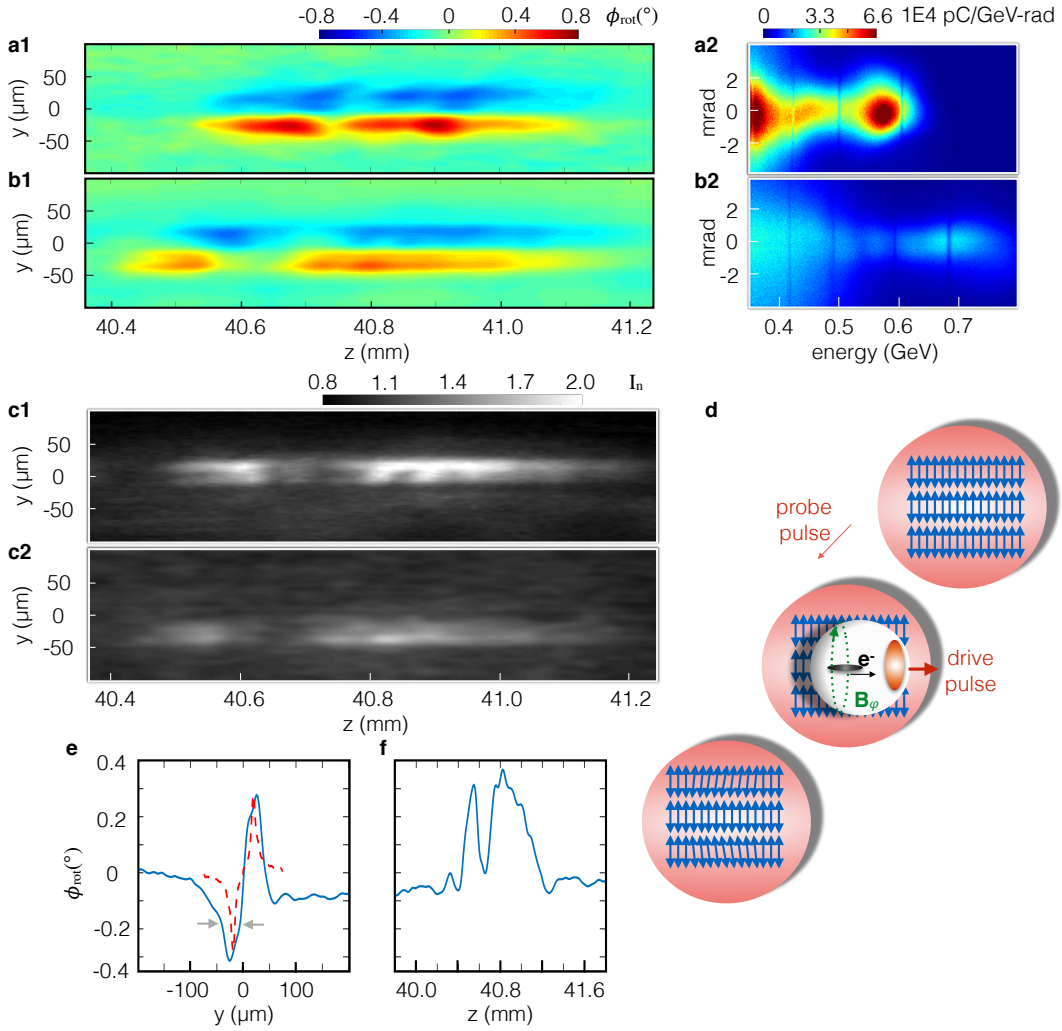

Figure 3.3: **The Faraday rotation signal of stabilized bubbles** (**a1**, **b1**), Faraday rotation angle induced by stabilized bubbles. (**a2**, **b2**), The electron spectra of (**a1**) and (**b1**), respectively. The total charge above 300 MeV is 45.65 pC on a2, and 13.46 pC on b2. (**c1**, **c2**), The normalized signal images that were used to generate b1. The procedures of image normalization and rotation angle calculation can be found in Methods 3.4.1. (**d**), The cartoon of the Faraday effect induced by the plasma bubble which occurs prefrentially around the region that overlaps with the bubble wall. (**e**), The blue solid line is the vertical line-out of (**b1**) averaged from $z = 40.07$ to 41.1 mm. The red dashed line is the result of the FDTD simulation. The width (FWHM) of the peak is 35 μm. (**f**), The horizontal line-out of (**b1**) averaged from $y = -40$ to 0 μm.

imaging system can be found in Methods 3.4.2.

The Faraday rotation signals of the stabilized plasma bubble are shown in Fig. 3.3. The zero point of the z-axis is the entrance of the gas cell, and the drive pulse propagates from left to right. The color scale on the rotation angle data shows the magnitude and the direction of the rotation, and the region where the Faraday effect is the strongest is symmetric around the laser axis (Fig. 3.3a1 and b1). The long streak feature of the signal is due to the long pulse length of the probe pulse, and the negative and positive rotation means that the magnetic field is pointing into($\hat{x}$) and out of ($-\hat{x}$) the page, respectively. Since the Faraday effect is induced by the coupling of the magnetic field and plasma density, the magnitude of the rotation angle should be at its maximum around the region of the dense plasma around the bubble walls (see Discussions). Hence the distance between the peaks and valleys indicates the transverse size of the plasma bubble. The vertical line-out (Fig. 3.3e) of the rotation angle signal agrees reasonably with the FDTD simulation, which shows that the Faraday rotation happened dominantly around the bubble walls. The average transverse distance between the peaks and the valleys of the rotation angle is $\simeq 50.8 \pm 10.1$ μm, which matches the diameter of the plasma bubble ($2R_b = 2\sqrt{a_0}/k_p \simeq 56.4$ μm, where R_b is the radius of the plasma bubble, $a_0 \simeq 3.5$ is the normalized vector potential [2], and $k_p = 0.13$ μm^{-1}). Furthermore, the Faraday rotation signals were observed only in conjunction with accelerated electrons, and the magnitude of the rotation angle increased when the electron bunch had more charge. For instance, in Fig.

3.3a1, the peak value of the rotation angle is 0.7°, and the total charge of the accelerated electron bunch above 300 MeV is 45.65 pC. While in Fig. 3.3b1, the maximum rotation is 0.45°, and the total charge of the electron bunch above 300 MeV is 13.46 pC. The result has shown that the plasma bubble is indeed stabilized at $z \sim 40$ mm, in agreement with the simulation[14]. Moreover, obtaining Faraday rotation signal of LPA in low density plasma has been proven possible.

3.2.2 Faraday rotation signal of evolving bubble

After the major upgrade of the Texas Petawatt[37], the focus of the drive pulse was greatly improved (typical Strehl ratio > 0.6), and we consistently obtained multi GeV electrons with charges up to nC. In order to study the bubble evolution in the early stage, we sent four probe pulses, with pulse length ~ 500 fs and diameter ~ 1 cm, to obtain the movies of the bubble in a single shot. Since the drive pulse is focused with a mismatched geometry ($R_L \approx 2.8 R_{sg}$, where $R_{sg} \approx 29$ μm), intended to generate bubble oscillations and self-injections[14], complicated structure of Faraday rotation angle in the early stage of the acceleration is expected. The distance between the probe pulses (from center to center) was around 9.5 mm (see Fig. 3.4a), and they covered around 4 cm interaction region in the gas cell. The long pulse length of the probe pulses not only reduced the difficulty of the temporal overlapping of the probes and the drive pulse, but also minimized the pulse length variation after propagating through the substrates (*e.g.* windows and beamsplitters).

The details of the setup of the probe pulses can be found in Methods 3.4.3.

Faraday rotation signals revealing the plasma bubble evolution are shown in Fig. 3.4. The longitudinal distance between the signals is around the distance (± 200 μm) between the probe pulses, which further verifies that the signal is sensitive to the pump probe overlap (see Fig. 3.4a). Note that the magnification ratio of the vertical and the horizontal axis of Fig. 3.4b1 and b2 (the signal on probe 1) is adjusted to $15:1$.

On probe 1, the signal at $z = 14.0$ mm on camera A-1 (Fig. 3.4b1) is where the Faraday rotation induced by the plasma bubble expected to be, but the signal saturated camera A-2 (Fig. 3.4b2). In order to detect the wave breaking radiation, we have to adjust the filter on camera A-1 and A-2. As a result, sometimes the Faraday rotation signal on probe 1 is not attainable. Nevertheless, wave-breaking radiation[38] is observed at $z = 12.15$ and 16.68 mm on both images, which indicates that self-injection[26] happens in this region, in agreement with the previous observation[2].

On probe 2, 3, and 4 (Fig. 3.4c, d, and e), the transition from bubble oscillation to stabilization is observed in a single shot. In addition, the accelerated electron bunch has small divergence (FWHM 1.86 mrad, see Fig. 3.4f), and high electron charge with ~ 1.12 nC above 300 MeV (82.25% of total charge in the bunch, see Fig. 3.4g), as predicted by the simulation [14]. The high electron charge is responsible for the large magnitude of the Faraday rotation angle when the bubble is stabilized (up to 10° at $z = 42.43$ mm). The signals on probe 2 and 3 appear to be more complicated than the calcu-

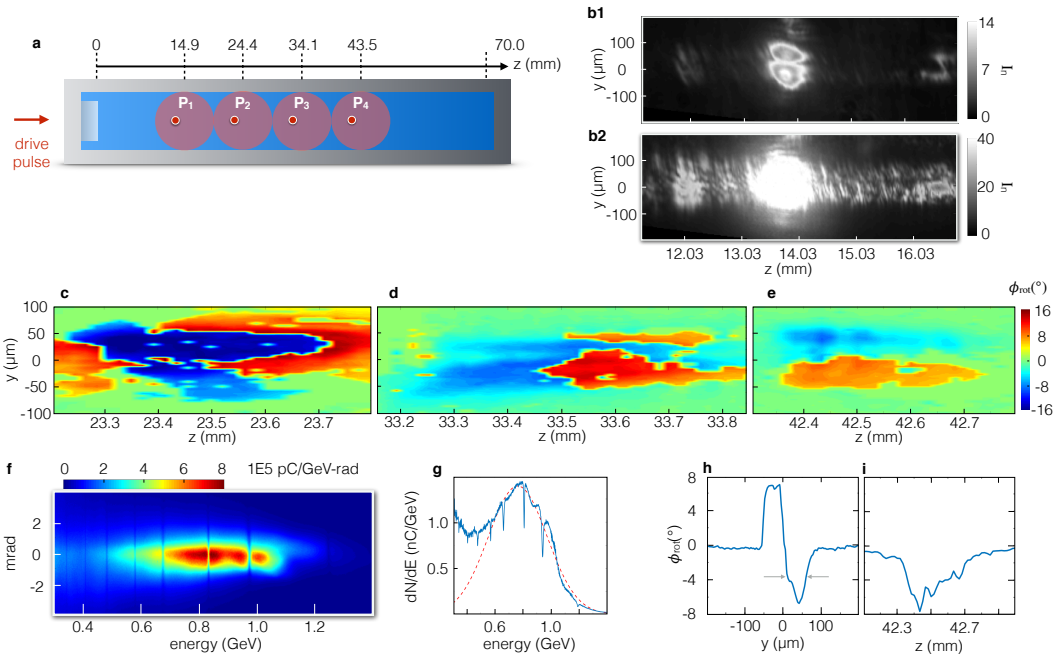

Figure 3.4: **The Faraday rotation signal of an evolving bubble** (**a**), The side view of the gas cell and the position of the probe pulses. The white circles on the probes indicate the location of the Faraday rotation signals. (**b1**, **b2**), The images on probe 1 normalized to the background captured by camera A1 and A2, respectively. The signal at $z = 14.0$mm is where the bubble should overlap with the probe pulse, and the signals at $z = 12.15$ and 16.68 mm are wave-breaking radiation. (**c-e**), The Faraday rotation angle on probe 2, 3 and 4. (**f**), The electron spectrum from this shot. The divergence of the electron bunch is 1.86 mrad. (**g**) The electron spectrum integrated over divergence. The total charge above 300 MeV is 1.12 nC, and 82.25% of total charge is in the energetic bunch (red dashed line, Gaussian fit of the peak). (**h**) The averaged vertical line-out in from $z = 42.48$ to 42.72 mm on (**e**). The width (FWHM) of the valley is 57 μm. (**i**), The averaged horizontal line-out from $y = 20$ to 50 μm on (**e**).

lated results, which may be associated with the non-uniformity of the drive pulse focusing[2], bubble evolution and asymmetry, and electron side and back ejections[39]. Although the distribution of Faraday rotation angle is complicated in probe 2 and 3, one can still find the region of interest on Fig. 3.3c, d, and e along the laser axis where the rotation angle implies the formation of the plasma bubble. The region of interest locates at the expected location of the plasma bubble, and longitudinal range of the region is ~ 200 μm (the length of the overlapping trace between the bubble length and the probe pulse). On probe 2 (Fig. 3.3c), the region of interest is 23.5 mm $< z <$ 23.7 mm. On probe 3 (Fig. 3.3d), the region of interest is 33.4 mm $< z <$ 33.6 mm, and on probe 4 (Fig. 3.3e), the region of interest is 42.4 mm $< z <$ 42.6 mm. In those regions right beside the laser axis, the averaged vertical distances between the peaks and valleys of the rotation angle are 29 μm on probe 2, 41 μm on probe 3, and 60 μm on probe 4. The increasing distance between the peaks and valleys indicates that the bubble is gradually stabilized (see Discussion) until it passes $z = 42.5$ mm.

3.3 Discussion

3.3.1 Faraday rotation simulations using FDTD - stabilized bubble

In order to demonstrate that the Faraday rotation signal can reveal the plasma bubble structures, we performed a series of finite difference time domain (FDTD) simulations (see Methods 3.4.4). In the FDTD simulations, we sent a plane wave through static dielectric structures of the plasma bubble.

The parameters of the dielectric structures were taken from a cylindrically symmetric PIC wakefield simulation [2],[14]. The PIC simulation was performed using WAKE[40], a fully relativistic PIC code in axisymmetric geometry. (see Fig. 3.5)

Ideally, to obtain the Faraday rotation accurately, one needs to solve the eigenmodes and the dispersion relations of each grid and calculate the overall rotation (we call it ϕ_1) of the polarization of the probe beam after propagating through the magnetized plasma. However, solving eigenmodes and dispersion relation for each grid is time-consuming and not practical in simulations.

To simplify the problem, we considered only the $\mathbf{B}_\varphi \cdot \hat{\mathbf{k}}$ component of the magnetic field, where $\hat{\mathbf{k}}$ denotes the normalized wave vector of the probe beam (in our case, $\hat{\mathbf{k}} = \hat{\mathbf{x}}$), so the dielectric constant can be simplified as

$$\tilde{\epsilon}_r^{\pm} = 1 - \frac{\tilde{\omega}_p^2}{\tilde{\omega}(\tilde{\omega} \pm \tilde{\Omega}_B)}, \tag{3.2}$$

where $\tilde{\Omega}_B = e \cdot \tilde{B}_\varphi cos(\theta)/m_e$ is the cyclotron frequency, θ is the angle between $\tilde{\mathbf{B}}_\varphi$ and $\hat{\mathbf{k}}$, $\tilde{\omega}_p = \sqrt{\frac{\tilde{n}_e e^2}{\epsilon_0 m_e}}$ is the plasma frequency, $\tilde{\omega}$ is the frequency of the probe beam, and $\pm$ represents the right-handed and left-handed circularly polarized eigenmodes. The symbol $\sim$ denotes that the quantities are in the plasma rest frame. The rotation angle can now be written as

$$d\tilde{\phi}_2 = \frac{\tilde{\omega}}{c}\left(\sqrt{1 - \frac{\tilde{\omega}_p^2}{\tilde{\omega}(\tilde{\omega} - \tilde{\Omega}_B)}} - \sqrt{1 - \frac{\tilde{\omega}_p^2}{\tilde{\omega}(\tilde{\omega} + \tilde{\Omega}_B)}}\right)dx \tag{3.3}$$

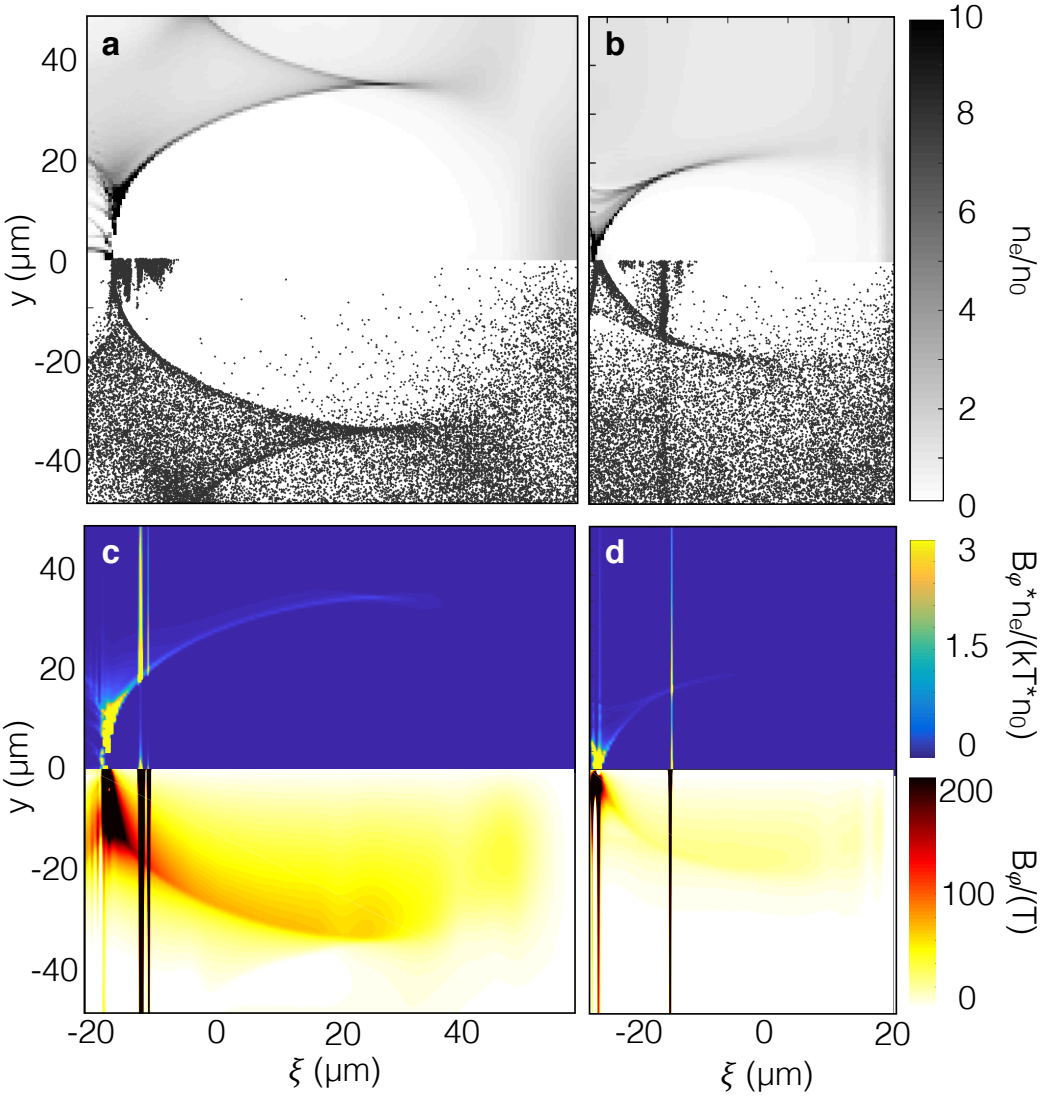

Figure 3.5: **Simulation data from a cylindrically symmetric PIC code, WAKE.** (**a**, **b**), Plasma density (upper half) ($n_0 = 4.8 \times 10^{17}$ cm^{-3}) and test particle distribution (lower half). (**c**, **d**), $B_\varphi \cdot n_e$ (upper half) and B_φ (lower half) of the bubble. (**a**, **c**), Immediately after the self-injection happens. (**b** ,**d**), 6 cm downstream after self-injection.

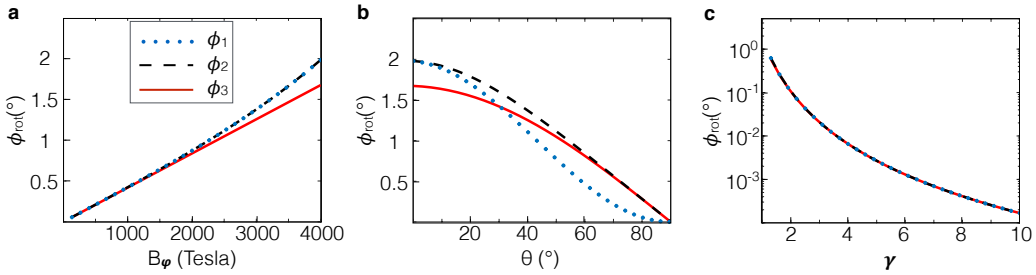

Figure 3.6: **Faraday rotation angle calculated by different methods.** ϕ_1 is the obtained by finding the eigenmodes and solving the dispersion relations. ϕ_2 is calculated by Eq. (3.3), and ϕ_3 is calculated by Eq. (3.4). (**a**), ϕ_{rot} versus the magnitude of the magnetic field. $\theta = 0°$. The plasma thickness is $\Delta x = 50$ μm. (**b**), ϕ_{rot} versus the angle between $\mathbf{B}_\varphi$ and $\hat{\mathbf{k}}$. $B_\varphi = 4000$ Tesla. $\Delta x = 50$ μm. (**c**), ϕ_{rot} versus the Lorentz factor of the plasma flow. $\theta = 0°$, and $B_\varphi = 4000$ Tesla. $\Delta x = 50$ μm.

Here, dx represents an infinitesimal step of the probe beam.

Furthermore, when $\tilde{\Omega}_B \ll \tilde{\omega}$, Eq. (3.3) can be approximated by

$$d\tilde{\phi}_3 = \frac{\tilde{\omega}_p^2 \cdot \tilde{\Omega}_B}{2\tilde{\omega}^2 c} dx, \tag{3.4}$$

which has been used to obtain the expression of Eq. (3.1). The comparison of different methods of obtaining Faraday rotation angle (ϕ_1, ϕ_2, and ϕ_3) is shown in Fig. 3.6. Although ϕ_2 is not exactly the analytical solution ϕ_1, it is easier to calculate, and it slightly deviates from ϕ_1 only when θ is close to 90° where the rotation is already small. Therefore, in the following FDTD simulations, we will use Eq. (3.2) to calculate the dielectric constant. Since the data of the PIC simulation are in the lab frame, we are going to simplify the problem and ignore the difference between the plasma rest frame and the

lab frame, and we will discuss the difference afterwards.

In the first step, we performed two 2D FDTD simulations. We took a slice of the plasma bubble at the location of the accelerated electron bunch from the PIC simulation ($\xi = \xi_0 = -17$ μm in Fig. 3.5a and c) , calculated the dielectric distribution of the bubble slice, namely, $\epsilon_r^{\pm}(x, y, \xi = \xi_0) = 1 - \frac{\omega_p(x,y,\xi=\xi_0)^2}{\omega(\omega \pm \Omega_B(x,y,\xi=\xi_0))}$, and sent a plane wave through the dielectric structure. The plane wave propagated along x-axis and was linearly polarized along the y-axis. The wavelength of the plane wave was 1.054 μm, the same as the probe beam in the experiment.

In order to reveal the connection between the Faraday rotation signal and the thickness of the bubble walls, we varied the thickness and the plasma density of the bubble wall while kept the total particle numbers conserved. The FWHM of the bubble wall were 1.64 and 8.23 μm, and the peaks of the densities were 7.4 and 1.48×10^{18} cm^{-3} respectively.

Fig. 3.7 shows the results of the 2D FDTD simulations. The plane wave propagates from left to right, and the polarization of the beam is along the y-axis. The color scale shows the polarization rotation of the probe beam (Fig. 3.7a1 and b1), and the lineout plots (Fig. 3.7a2 and b2) show the rotation angle signals imaged at the center of the bubble by a nearly perfect ($f/0.08$) imaging system.

In Fig. 3.7b1 and b2, we chose two different object planes, one at the center of the bubble (in-focus, blue line) and the other one 30 μm downstream

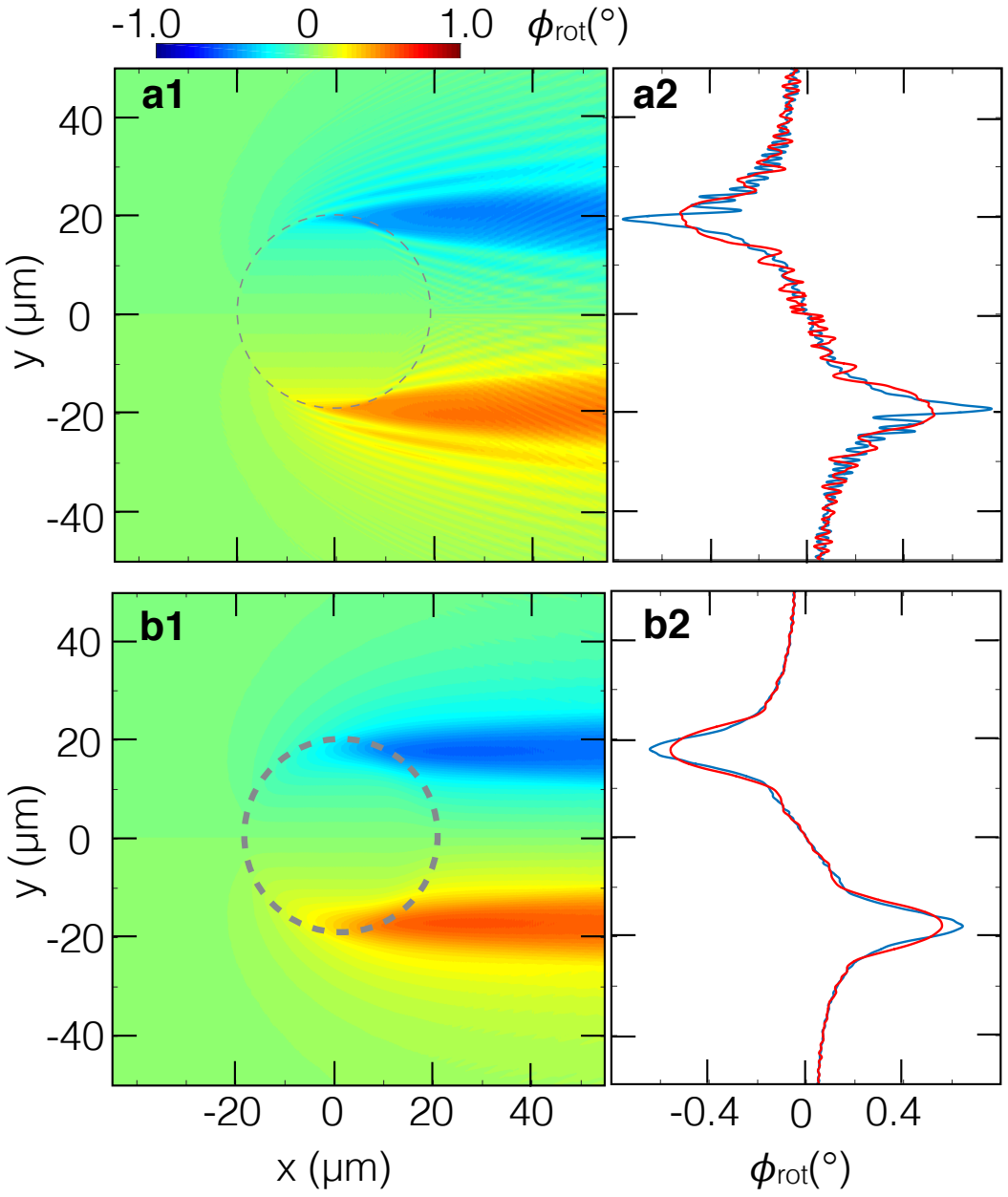

Figure 3.7: **2D FDTD simulation results**. (**a1**, **b1**), 2D FDTD Simulation of the Faraday rotation induced by the plasma bubbles. The thickness of the the bubble walls are 1.64 and 8.23 μm respectively. (**a2**, **b2**), Line-outs of the simulated rotation angle signals imaged by a near perfect imaging system (f/0.08). The object planes are on the center of the plasma bubble (in-focus, blue lines) and 30 μm downstream (out-of-focus, red lines).

(out-of-focus, red line). The out-of-focused rotation angle signal was diffracted (Fig. 3.7b2 red lines) when the thickness of the bubble wall was close to the wavelength of the probe beam. In both cases, the distance between peak and valley of the rotation angles matches the diameter of the plasma bubble, which proves that Faraday rotation corresponds to the location the bubble walls.

3.3.2 Faraday rotation simulations using FDTD - bubble transition

To demonstrate the transition of the Faraday rotation signal induced by an evolving bubble and a stabilized bubble, we extended the 2D simulation and performed two 2D+1 FDTD simulations . We took two different bubble parameters from the PIC simulation. The first bubble parameter was immediately after the self-injection happened (Fig. 3.5a). This was in the first stage of the acceleration process. The other bubble structure was 6 cm downstream after self-injection happened where the bubble stabilized (Fig. 3.5b). This was the second stage of the acceleration process.

We calculated the dielectric distribution of the bubble as $\epsilon_r^{\pm}(x, y, \xi) = \sum_i \epsilon_r^{\pm}(x = x_i + \xi, y, \xi)$, and sent a plane wave along $x = \xi$ axis, which means that the plane wave overlapped with the bubble with 45°, as how the probe beam actually overlapped with the bubble in the experiment. Here, $\{x_i\}$ are the pixels on the x axis from the PIC simulation. Similar to the 2D simulation, the probe beam was linearly polarized in y-axis. The difference here is that, instead of using a thin plane wave, we added a pulse length to the probe beam where $\tau_L = 100$ fs.

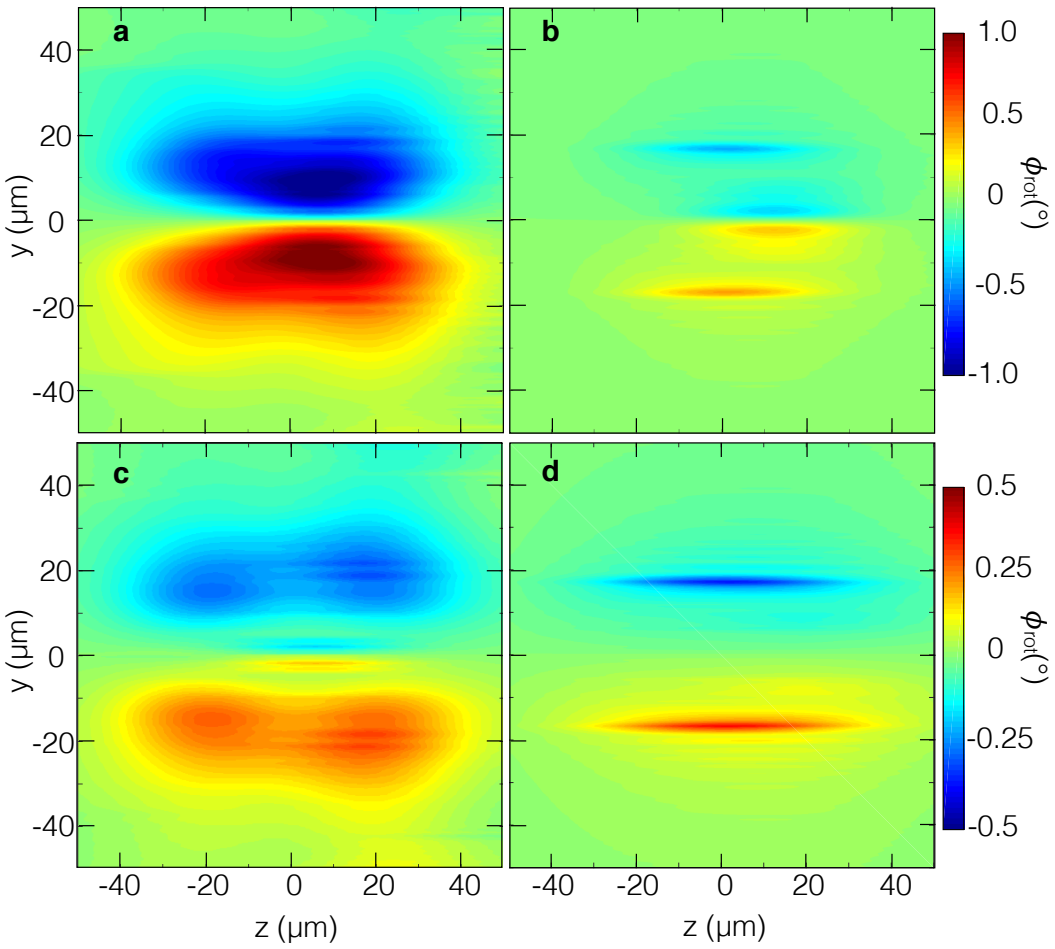

Figure 3.8: **Faraday rotation signals from 2D+1 FDTD simulation.** (**a**), The rotation angle of the probe beam after propagating through the bubble in the first stage of the acceleration. (**b**), The rotation angle of the probe beam after propagating through the bubble in the second stage of the acceleration. (**c**), The rotation angle of the first stage after considering the relativistic effect. (**d**), The rotation angle of the second stage after considering the relativistic effect.

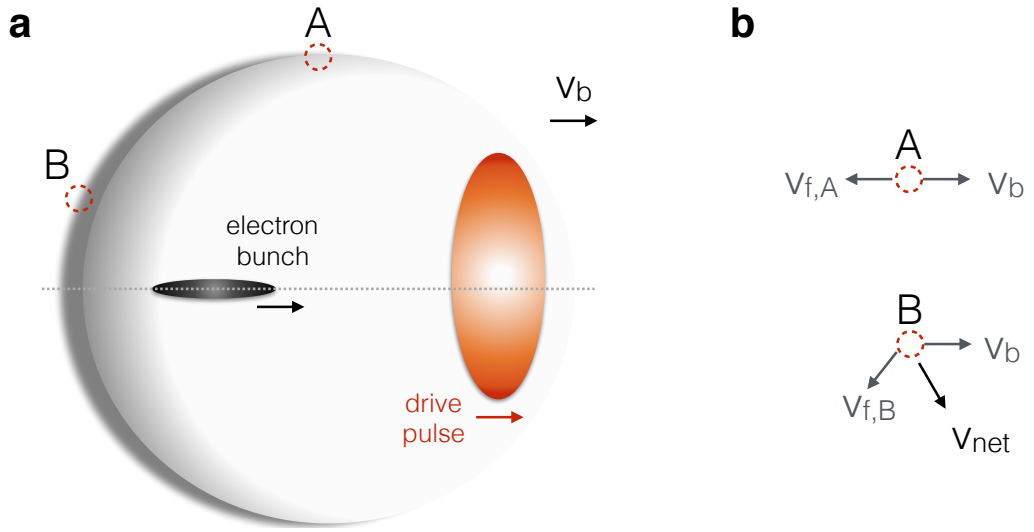

Figure 3.9: **Diagram of plasma bubble and the plasma flow.** (**a**), plasma bubble induced by a laser pulse. (**b**), qualitative explanation of the plasma net flow at different positions of the bubble wall in the lab frame.

In the first stage of the acceleration, large amounts of electrons, both passing electrons and injection candidates, aggregate on the back of the bubble ($n_e \sim 1 \times 10^{19}$ cm^{-3}) . Moreover, about 98% of the electrons in the back of the bubble have forward momentum $P_z/(m_e c) > 10$ because they experience long slippage time around the bubble[28]. Therefore, the electrons on the back of the bubble induce a strong azimuthal magnetic field (> 500 T) (Fig. 3.5c, bottom half). As a result, the injected electrons contribute little to $B_\varphi \cdot n_e$ (Fig. 3.5c, top half) even though the magnetic field induced by them is > 300 T on the bubble wall. In the second stage of the acceleration, however, the electron aggregation on the back of the bubble reduces, and the azimuthal magnetic field is less intense on the back of the bubble (Fig. 3.5d, bottom

half). Consequently, the contribution of the accelerated electron bunch to $B_\varphi \cdot n_e$ is more significant (see Fig. 3.5d, top half).

Fig. 3.8 shows the simulated Faraday rotation signals of the probe beam after propagating through the bubble. In the first stage of the acceleration (Fig. 3.8a), the vertical width of the signal is thick (FWHM $\sim$ 18 μm), and the peak of the signal is close to the laser axis due to the dense and thick plasma wall and strong magnetic field on the back of the bubble (see Fig. 3.5(c)). In the second stage, the vertical width of the peak becomes $\sim$ 4 μm. The maximum of the rotation angle is located at $\sim$ 17.4 μm above the center (Fig. 3.8b), while the intense region of $B_\varphi \cdot n_e$ induced by the accelerated electron bunch is 16.58 μm above center (Fig. 3.5d, upper half), which shows that the contribution of the electron bunch is more relevant in the second stage. Therefore, in the second stage, due of the reduction of $B_\varphi \cdot n_e$ on the back of the bubble, the location of the maximum of the rotation angle can better represent the transverse size of the bubble. However, the experimental results didn't show significant peak close to the laser axis when bubble was stabilized (Fig. 3.3a1 and b1), while the simulation (Fig. 3.8b) show some signal near the center. The discrepancy of the experiment and simulation can be explained by considering the relativistic plasma flow of the bubble.

3.3.3 Relativistic effect on Faraday rotation signals

So far in the FDTD simulations, we assumed that the plasma bubble was static, and we used the data from the PIC simulation, which were in the lab

frame, to calculate the dielectric constant ϵ_r. However, in reality, part of the plasma bubble (especially the back of the bubble) reaches relativistic velocities along with the drive pulse. Therefore, we need to include the relativistic effect to calculate the dielectric constant in the plasma rest frame.

To calculate the dielectric constant in Eq. (3.2), we need to convert three quantities from the lab frame to the rest frame of plasma [30]. The first one is the plasma density, $\tilde{n}_e = n_e/\gamma$. The second one is frequency of the probe beam, $\tilde{\omega} = \gamma(1 - \beta \cdot \hat{\mathbf{k}})\omega$, and the third one is the magnetic field, $\tilde{\mathbf{B}}_\varphi = (\mathbf{1} + \gamma^2\beta\beta) \cdot \mathbf{B}_\varphi/\gamma$. Here γ is the Lorentz factor and β is the velocity of the plasma flow. After considering the relativistic effect of the plasma flow, the rotation angle ϕ_{rot} is proportional to $1/\gamma^4$ as shown in Fig. 3.6c.

The result of FDTD simulation with the relativistic effect of the plasma flow is shown in Fig. 3.8c and d. In Fig. 3.8c, the magnitude of the rotation angle decreases drastically due to the relativistic effect. In particular, the rotation angle close to the laser axis is suppressed the most. Nevertheless, the vertical width of the rotation angle is still wide. The data in Fig. 3.8d, however, shows almost no rotation in the region close to the laser axis, while the amount of the rotation away from the laser axis is nearly unchanged. The reason can be explained as follows.

Suppose that the bubble propagates through the plasma with velocity v_b (see Fig. 3.9). Electrons in the bubble wall flow around its periphery with velocity v_f in the bubble's rest frame. In a non-relativistic calculation for a "stable" bubble (Fig. 3.8b), streaming electrons at the side wall (position A

on Fig. 3.9a) of the bubble contribute the outer Faraday shift lobe (~ 20 μm from axis), whereas streaming electrons at position B of Fig. 3.9a near the back of the bubble (5 to 10 μm from axis) contribute the inner lobe, which is not observed in the experiments. In the lab frame (where the measurement is made), electrons at the side wall have velocity $v_b - v_{f,A} \sim 0$ (see Fig. 3.9b), whereas electrons at the back of the bubble have velocity $v_{net} \sim 0.97c$ ($\gamma \sim 4$) given by the vector sum of v_b and $v_{f,B}$. Consequently the Faraday rotation from these electrons is suppressed by a factor $1/\gamma^4 \sim 1/256$. This explains the relative weakness of the shift near the propagation axis.

By comparison, the Faraday rotation signal from the first stage(Fig. 3.8c) is similar to the data shown in Fig. 3.3c in terms of the wide vertical width. In the second stage (Fig. 3.8d), the narrow vertical width of the rotation angle signal and the bigger zero rotation region between the peak-and-valley are better resembled in the data in Fig. 3.3e, which is ~ 20 mm further downstream than Fig. 3.3c.

To summarize, we demonstrate the movies of evolving plasma bubble of GV-class LPAs using Faraday rotation multiplexing in a single shot. The signal shows that the mismatch focusing of the drive pulse ($R_L \approx 2.8 R_{sg}$) produces a strongly dynamic plasma bubble in the early stage of the acceleration, which generates high charge electron bunches (~ 1.12 nC) due to bubble oscillation induced self-injection[14],[13], and the bubble becomes stable after over 20 mm propagation. The study of the Faraday rotation induced by oscillating bubbles requires further investigations.

3.4 Methods

3.4.1 rotation angle evaluation

To calculate the rotation angle, we first normalize the signal images using the null images (the probe pulse images with no drive pulse). To do so, we use a Matlab function called "imregister" to register the null images and the signal images. The "imregister" function iterates and optimizes (using translation, rotation, and scaling) registering the intensity based images until the error is within a tolerable range. We then divide (normalize) the intensity of the signal images to the null images. After normalization, the region with no signal (no rotation) should be 1 (If not, one has to multiply the image to a certain ratio). The normalized intensity $\bar{I}_i(y,z)$ can be described as

$$\bar{I}_i(z,y) = (1-\beta_i \cdot cos^2(\phi_{rot}(z,y)-\theta_i))/(1-\beta_i \cdot cos^2(\theta_i)), \qquad (3.5)$$

where β_i is the extinction ratio of the polarizers, $(1-\beta_{A-1}) = 4.9\times10^{-3}$, $(1-\beta_{A-2}) = 3.2\times10^{-3}$, $(1-\beta_{B-1}) = 21.1\times10^{-3}$, and $(1-\beta_{B-2}) = 3.3\times10^{-3}$. θ_i is the biased angle of the polarizers in front of the cameras, where $\theta_{A-1} = 2.0^\circ$, $\theta_{A-2} = -2.0^\circ$, $\theta_{B-1} = 2.1^\circ$, and $\theta_{B-2} = -2.1^\circ$.

Furthermore, we use the Matlab "imregister" function to register the images of camera A-1 and A-2 (and similarly, B-1 and B-2). After registering the images, the rotation angle $\phi_{rot}(z,y)$ can be found by solving $\bar{I}_{A-1}/\bar{I}_{A-2}$, which is monotonic in $\pm3.5^\circ$ (for $\bar{I}_{B-1}/\bar{I}_{B-2}$, the monotonic range is $\pm2.7^\circ$).

When the rotation angle is beyond the monotonic range, to avoid am-

biguity when solving ϕ_{rot}, we define a tolerance measure δ, where

$$\delta(\bar{l}_{A-1}, \bar{l}_{A-2}) = \sqrt{(\frac{\bar{l}_{A-1} - \bar{l}^0_{A-1}}{\bar{l}^0_{A-1}})^2 + (\frac{\bar{l}_{A-2} - \bar{l}^0_{A-2}}{\bar{l}^0_{A-2}})^2}. \tag{3.6}$$

Here, $\bar{l}^0_i = (1 - \beta_i \cdot cos^2(\phi^0_{rot} - \theta_i))/(1 - \beta_i \cdot cos^2(\theta_i))$ where ϕ^0_{rot} gives the minimum δ. In other words, ϕ^0_{rot} is the value that is closest to the theoretical rotation angle and can be used as the solution. The details of solving the rotation angle beyond monotonic range can be found in the supplementary information.

3.4.2 The imaging system

The relay imaging system right next to the gas cell is composed of two 3" wide achromat lens from Edmund Optics. The anamorphic imaging system consisted of three lenses. The first lens is an 2" spherical achromat doublets with 15 cm focal length. The second lens is a 1" achromatic cylindrical lens with 25 cm focal length to magnify the vertical dimension. The third lens 3 is a 1" achromatic cylindrical lens with 5 cm focal length to demagnify the horizontal dimension. The anamorphic image is very close to the last cylindrical lens ($<$ 5 cm), so we used a 2" wide achromatic doublet pair (f=20 cm each) to relay image the beam to the cameras. All three lenses in the anamorphic imaging system and the achromatic doublet pair are from Thorlabs. Furthermore, in order to make sure that the axis of the lenses are properly aligned, all lenses (including the achromatic doublet pair after the anamorphic system) are mounted on a cage system bought from Thorlabs. The horizontal field of

view of the imaging system was $\sim$ 29.4 mm, and the vertical resolution was $\sim$ 8.8 μm (see Fig. 3.2). The vertical resolution was determined by averaging the distances between the horizontal lines of the elements on the image of a USAF target, and 8.77 μm (group 5 element 6) was the smallest distance that could be resolved on the image. The depth of field was up to 300 μm (Fig. 3.2b).

3.4.3 The probe pulse sampling

The probe pulses were generated through a beam sampler, composed of two 2" wide beamsplitter (80R/20T and 70R/30T) and a 4" wide metal mirror (see Fig. 4.1a). The metal mirror was oriented 45° to the beam path of the drive pulse so that the probe pulses could propagate perpendicularly to the drive pulse. If the first probe pulse overlapped with the drive pulse in the gas cell, as long as the probe pulses were parallel to each other, all the following probe pulses should overlap with the drive pulse as well. The probe pulses were divided to two groups using two metal mirrors, and each group was imaged by an anamorphic imaging system onto the polarimetry analyzing setup.

3.4.4 Finite difference time domain method simulations

The FDTD simulations use 1000×2000 grid cells with $dx = dy = 0.05$ μm. The EM wave propagates in x direction and is linearly polarized in y direction. We use uniaxial perfect match layer (UPML) as the boundary

absorber with 10 grid cells in the perfect match layer. The dielectric structures of the FDTD simulation is derived from the plasma density of a cylindrically symmetric PIC simulation, WAKE (see Wang *et al.*'s report[2]). The FDTD simulation was executed in Stampede, a super computer at Texas Advanced Computering Center (TACC).

Chapter 4

Single-Shot Observation of Time-Resolved Pulse Propagation in Glass

4.1 Introduction

[1]

Propagation of ultrashort pulses in transparent materials can induce significant nonlinear effects on the temporal, spectral, and spatial profile of the pulses. Theory [41] and simulation [42] have shown that when the pulse power is above the critical power for self-focusing (P_{cr}), the pulse will undergo dramatic collapse.

Chernev et al.[43] performed a simulation based on the Nonlinear Schrodinger equation (NLSE), and discovered that when a pulse propagated in normal dispersive material, it temporally split into two symmetric pulses. In that paper, they suggested that the splitting was caused by strong diffraction of the peak of the pulse in the presence of group velocity dispersion (GVD).

[1]The first author Y.-Y. Chang is responsible for performing the experiment. The experiment is initiated by Z. Li, and the simulation is conducted by J. Gulley. J. Welch helps taking the data. R. Zgadzaj, A. Bernstein, and M. Downer contribute to the general experimental design and data analysis. This work is under reviewing process with Optics Letters.

Experiments have also provided evidence of pulse temporal splitting in glass. For instance, Diddams et al.[44] measured the temporal profile of pulses propagating through 2.5 cm fused silica and discovered, using SHG-FROG, that temporal splitting occurred when the pulse power $P > P_{cr}$. Multiple reports have suggested that MPI and plasma defocusing is the main cause of pulse temporal splitting in solids. For example, Ranka et al. [45] revealed a close connection between supercontinuum generation (SCG) and pulse temporal splitting in a BK-7 glass window, which indicates that plasma generation may play a key role in pulse splitting. Moreover, Tzortzakis et al. [46] suggested that the mechanism behind the robust filament is the balance between self-focusing and multiphoton ionization (MPI).

In order to fully reveal pulse propagation in transparent materials in single shot, our group has developed a series of spectral interferometry techniques. In frequency-domain holography (FDH)[22], we sent frequency-doubled probe and reference pulses propagate co-linearly with the pump pulse and obtained a snapshot of the pump-induced phase structure in a dispersive material. Using a frequency-domain streak camera (FDSC) [24], we extended FDH by introducing an oblique angle between the beam paths of the pump and the probe pulse. Since the group velocity of the pump and the probe are different, the oblique angle converts a 2D phase streak to a time-resolved pump propagation in single-shot. Li et al.[24] have used FDSC to reveal a time-resolved process of pulse self-focusing in glass.

Using frequency-domain tomography (FDT), we apply multiple probe

pulses simultaneously to overlap with the pump with various angles and obtain a 2D movie of the pump pulse in a single shot. Li et al. [47] have used FDT to reveal that pulse collapsing in 3 mm fused silica was induced by plasma generation. Nevertheless, all the previous methods were not sufficient to resolve pulse temporal splitting because that the temporal resolution was limited by the bandwidth of the probe pulse. The temporal resolution of spectral interferometry techniques can be written as $\Delta t_{res} \sim (\Delta\omega)^{-1}[1+2\beta_2^2(\Delta\omega)^4]^{1/2}$ [48][49], where $\Delta\omega$ is the frequency bandwidth of the probe, $\beta_2 = 1/2(\partial^2\phi/\partial\omega^2)_{\omega_0}$ is the GVD of the probe. Therefore, in order to obtain the time-resolved process of pulse temporal splitting in single shot by using FDSC, one needs to broaden the bandwidth of the probe pulse (to increase $\Delta\omega$).

In this letter, we report single-shot, time-resolved observation of pulse propagation in 3 mm thick flint glass (SF11) using a broadband frequency-domain streak camera (B-FDSC). Unlike the conventional FDSC and FDT where the bandwidth of the probe pulse was $\sim$ 20 nm, we slowly focus the probe pulse through several thin coverslips, gradually broaden the bandwidth to $>$ 100 nm using supercontinuum generation while maintain a smooth pulse profile, which is crucial to FDSC technique. The temporal resolution of B-FDSC is $\sim$ 10 fs. Our measurement reveals the time-resolved dynamics of pulse self-steepening and temporal splitting in single-shot, which allows us to estimate the MPI coefficient of the medium. We perform a simulation that accounts for self-focusing, MPI, GVD, self-steepening, and space-time focusing effects to verify the experimental results.

4.2 Experimental Procedure

The schematic of the experimental setup is shown in Fig.4.1. To generate the broad bandwidth probe pulse, we slowly focused a 800 nm pulse (1 mJ, 40 fs) onto six 100 μm thick glass coverslips with $f/400$ [50]. We rotated each coverslip to the Brewster angle to yield the maximum transmission. The segmented material allows us to separate and control the self-focusing and self-phase-modulation, which is essential to obtaining a high optical quality pulse. Since the pulse self-focuses and diffracts through the medium, one has to finely adjust the positions of the coverslips to maintain the supercontinuum generation throughout the propagation. Moreover, since spectral interferogram requires a smooth spectrum, one has to adjust the distances between the coverslips to prevent strong spectral modulation of the pulse. As a result, we extended the bandwidth (ranged from 550 nm to 950 nm) of the pulse in a $\sim$ 20 cm device while maintained a smooth and symmetric pulse profile (see Fig.4.1(b)). We then sent the spectral-broadened probe pulse through a shortpass filter (cutoff at 670 nm) to select the blue-shifted bandwidth we needed for the experiment. The bandwidth of the pulse (FWHM $\sim$ 60 nm) should provide temporal resolution $\Delta t_{res} \sim$ 10 fs[48].

After the shortpass filter, we send the pulse through a piece of thick BK-7 to chirp the pulse to $\sim$ 500 fs and use a Michelson interferometer to generate a reference and a probe pulse for FDSC measurement[24]. The reference and the probe pulse propagate with an oblique angle ($\theta_0 = 11.95^\circ$ in the sample) to the pump pulse (800 nm, $\tau_L \approx$ 50 fs), which is focused on a 3-mm-thick glass

sample ($w_0 \approx 25.5\ \mu$m). The reference pulse arrives at the target slightly before ($\sim$ 1.2 ps) the pump pulse, but the probe pulse and the pump pulse arrive at the target simultaneously. The pump pulse then induces local refractive index change and imprints phase shift on the probe pulse. The spot size of the probe pulse is $\sim$ 2 mm, which is required to cover the full range of the pump pulse propagation in the glass target. The probing angle in the probe's co-moving frame is $\theta = 73.6°$ (see Fig. 4.2(a)), which means that the retrieved phase streak imprinted on the probe pulse should provide the evolution of the temporal profile of the pump pulse. The expression of angle conversion from lab frame to probe frame can be found in Li *et al.*'s paper [24].In order to acquire large phase shift induced by the pump pulse, we use SF11 as the sample material, which has high nonlinear refractive index ($n_2 = 9.5 \times 10^{-16}$ cm^2/W) and low $P_{cr} = \lambda_0^2/(2\pi n_0 n_2) \approx 0.6$ MW ($n_0 \approx 1.76$).

4.3 Experimental Results

The experimental results are shown in Fig.4.2. Each column from Fig. 4.2(b) to (d) represents a different pump pulse energy, ranging from 0.8 μJ to 2.4 μJ, and the peak intensity (I_0) of the pulse ranging from 0.78 to 2.34 TW/cm^2.The top row (Fig.4.2(b1)(d1)) is the line-out of the hologram data, and the second row (Fig. 4.2(b2) - (d2)) is the hologram data. The third row (Fig.4.2(b3)(d3)) is the phase streak extracted from the hologram, and the bottom row (Fig.4.2(b4)(d4)) is the spectrum of the pump pulse after exiting the glass sample. The phase streak in Fig.4.2 (b3) to (d3) evolves from top to

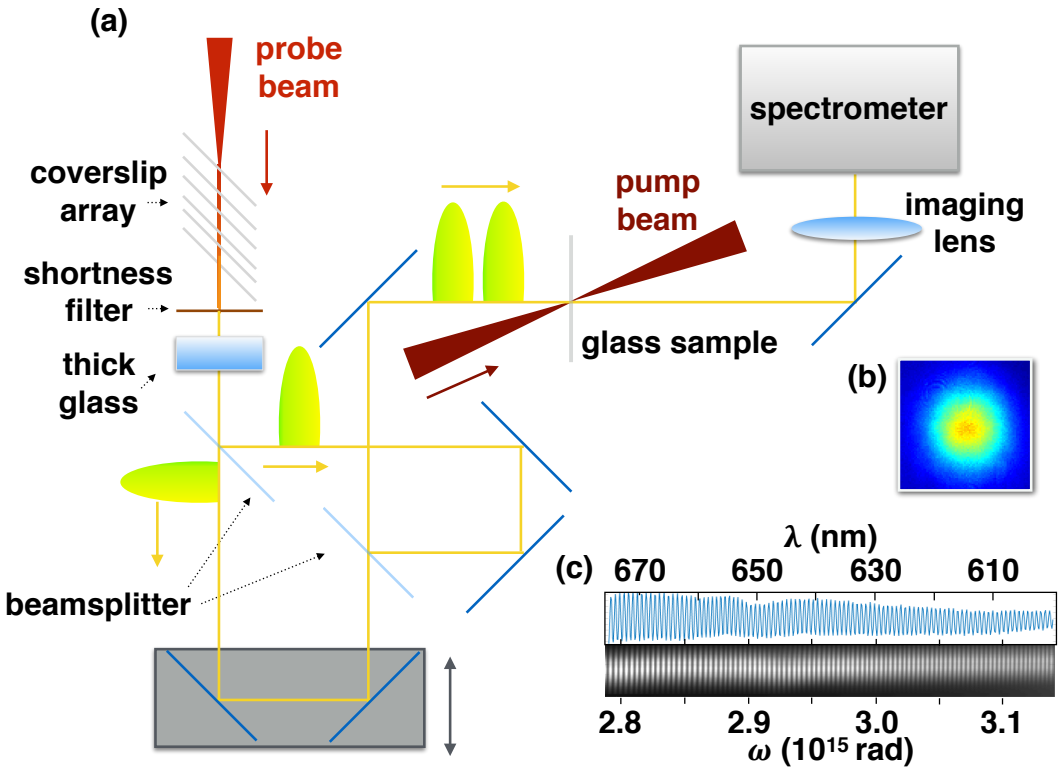

Figure 4.1: (a) The layout of the experimental setup. (b) The profile of the probe pulse. (c) The null spectral interferogram of the probe and reference pulses. The figure on top is the averaged line-out.

bottom. Since the probing angle (θ) in the probe's co-moving frame is close to 90°, the horizontal line-out of the phase streak represents the temporal profile of the object (the pump pulse). The vertical axis z represents the propagation distance of the object, and the left-hand side is the front of the object and the right-hand side is the back.

The trajectory of the phase streak, namely, the path of the peak, indicates the group velocity of the object. If the trajectory becomes shallower

toward the left, it means that the group velocity of the object becomes faster (hence red-shifted) because the object can "catch up" the front of the probe pulse more quickly. On the other hand, if the trajectory shows a steep angle, that means that the group velocity of the object is closer to that of the probe pulse, and the object would stay at the same temporal position on the probe pulse reference frame.

In the first case (Fig. 4.2(b3), where $I_0 \sim 0.78$ TW/cm^2, the intensity of the pump pulse increases gradually due to self-focusing, and the pulse length becomes narrower from $z = 1.6$ to 2.4 mm due to pulse steepening. The trajectory shows that the velocity of the peak intensity is slower than that of the trailing edge of the pulse, which agrees with the theory of self-steepening[51][52]. In the end of the propagation, the pulse broadens with a small peak at the front, which agrees with the red-shifted peak in the spectrum of the exit pulse (Fig. 4.2(b4)).

On Fig.4.2(c3) where $I_0 \sim 1.56$ TW/cm^2, the pulse self-focuses more quickly. The pulse length narrows briefly at $z = 1.6$ mm, and then the broadening takes over. At around $z = 2.2$ mm, the pulse starts to bifurcate into two pulses, and the trajectory of the larger pulse turns to the left significantly, which indicates that its the group velocity is faster than the incident pulse. The spectrum of the exit pulse (Fig. 4.2(c4)) also shows two main peaks. The red-shifted portion of the spectrum ranges from 900 to 800 nm, which corresponds to the leading pulse in Fig. 4.2(c3), and the blue-shifted portion of the spectrum corresponds to the trailing pulse in Fig. 4.2(c3).

Lastly, on Fig.4.2(f) where $I_0 \sim 2.34$ TW/cm^2, the pulse self-focuses in the beginning of the propagation and starts to broaden at $z = 1.1$ mm. The pulse then bifurcates into two pulses at $z = 1.8$ mm. The trajectories of the two pulses show different directions on the phase streak, which indicates that they separate further due to group velocity difference. One can estimate the group velocity of the pulse by

$$v_{ob} = v_{pr}[cos(\theta) - \frac{sin(\theta)}{cos(\theta)}\frac{v_{pr}}{m_s \cdot c}]^{-1},$$

where v_{pr} is the group velocity of the probe pulse in the sample, θ is the probing angle in the sample, $m_s = \Delta z/(c\Delta t)$ is the slope of the phase trace. Based on the trajectory of the phase streak, the center wavelength of the leading pulse is $\sim$ 820 nm, and that of the trailing pulse is $\sim$ 770 nm, in agreement with the exit spectrum of the pump pulse where it peaks at 776 and 813 nm.

4.4 Simulation

To understand the dynamics of pulse temporal splitting, we performed a 3D cylindrical symmetric simulations of pulse propagation in SF11. The simulations solve a unidirectional pulse propagation equation (UPPE) coupled with the density of electrons produced by MPI without avalanche ionization. We assume that the incident pulse was linearly polarized with central wavelength $\lambda_0 = 800\ nm$. The initial complex electric field of the pulse was

$$E(r, t, z = 0) = \sqrt{\frac{2I_0}{\epsilon_0 n_0 c}}\ \exp\left[-\left(\frac{r}{w_0}\right)^2 - \left(\frac{t}{\tau_0}\right)^2\right] \exp[-i\omega_0 t],$$

where z is the propagation axis, $n_0 = 1.76$ is the linear refractive index at the pulse center frequency, $I_0 = 1.8$ TW/cm^2 is the initial peak intensity, $w_0 = 30$ μm , and $\tau_0 = 50$ fs. The parameters in the simulation were chosen to match the pump pulse that generated pulse splitting in the experiment when it focused on the target. The laser pulse is evolved by numerically solving the UPPE in cylindrical coordinates [53]:

$$\begin{aligned} \partial_z \tilde{E}\left(k_\perp, \omega, z\right) &= i k_z \, \tilde{E}\left(k_\perp, \omega, z\right) + \\ &+ \frac{i\,\omega^2}{2\epsilon_0 c^2 k_z} \, \tilde{P}_{\text{NL}}(k_\perp, \omega, z) - \frac{\omega}{2\epsilon_0 c^2 k_z} \, \tilde{J}(k_\perp, \omega, z). \end{aligned} \tag{4.1}$$

Here, $\tilde{E}(k_\perp, \omega, z)$ is the Fourier-Hankle transformed electric field, z is the propagation axis, $k_\perp$ is the radial wavevector, ω is the frequency, $k_z = \sqrt{k^2(\omega) - k_\perp^2}$ is the z-component of the wave vector with magnitude $k(\omega) = n(\omega)\,\omega/c$, and $n(\omega)$ is the linear refractive index of SF11 as given by a Sellmeier equation.

In the SF11 sample we calculate the nonlinear polarization in the real space as

$$P_{\text{NL}}(r, t, z) = 2 n_0 \epsilon_0 n_2 I(r, t, z) E(r, t, z)\,, \tag{4.2}$$

where $I(r, t, z) = \frac{1}{2} n_0 \epsilon_0 c \, |E(r, t, z)|^2$ and $n_2 = 8.1 \times 10^{-20}$ m^2/W is the nonlinear refractive index, obtained by performing a z-scan separately.. The current density is given by $J(r, t, z) = J_f(r, t, z) + J_{\text{PI}}(r, t, z)$, where J_f and J_{PI} are the free current density and photoionization current, respectively.

The free current density is calculated by integrating the following coupled equations:

$$\partial_t \, \rho(r, t, z) = \sigma_K I^K(r, t, z) \left[\rho_{at} - \rho(r, t, z)\right] - \frac{\rho(r, t, z)}{\tau_r}, \tag{4.3}$$

$$\partial_t J_f(r,t,z) = \frac{e^2}{m}\rho(r,t,z)\,E(r,t,z) \tag{4.4}$$

Equation 4.3 is the evolution equation for the electron density, $\rho(r,t,z)$. The first term on the right hand side describes the photoionization contribution to the electron generation. Here, $\rho_{at} = 2.1 \times 10^{22}$ atoms/cm^3 is the atom density of the sample, K is the number of photons required for MPI, and σ_K is the MPI coefficient and is chosen to fit the data, which will be explained later. The effective band gap of the sample material is $U_i = 3.3$ eV [54], which means that $K = 3$ in our case. The second term on the right hand side accounts for electron recombination with a characteristic time $\tau_r = 25$ fs, which is obtained by performing the methods demonstrated by Sun et al. [55].

Equation 4.3 is the evolution equation of the free current density. Here, e is the electronic charge and the electron effective mass, $m = 0.95m_e$[54] (m_e is the electron mass), is related to the critical density $\rho_c = 1.8 \times 10^{21}$ cm^{-3} by $\rho_c = \epsilon_0 m\omega_0^2/e^2$, where ω_0 is the pulse central frequency. The photoionization current describes the time-averaged MPA and is given by

$$J_{\mathrm{PI}}(r,t,z) = n_0\,\epsilon_0\,c\,\beta^{(K)} I^{K-1}(r,t,z)E(r,t,z), \tag{4.5}$$

where $\beta^{(K)} = K\hbar\omega_0\sigma_K\rho_{at}$[46].

In order to determine σ_K, we estimate the multiphoton absorption length (L_{MPA}) of SF11 [56] defined as the length over which the intensity of the pulse I is attenuated by a factor of $[(K+1)/2]^{(K-1)}$. L_{MPA} can be written as

$$L_{MPA} = \frac{1}{2K\hbar\omega_0\sigma_K\rho_{at}I^{K-1}}$$

Based on the experimental results (Fig. 4.2(d3)), we estimate that L_{MPA} ranges from 50 to 500 μm, which means σ_K ranges between 0.6 and 6.4 $\times$ 10^7 $s^{-1}[TW/cm^2]^{-3}$. We run the simulation with different σ_K values (see Fig. 4.3 (c)), and we find out that when $\sigma_K = 6.72 \times 10^7$ $s^{-1}[TW/cm^2]^{-3}$, the pulse temporally splits into two pulses at $\sim$ 2 mm, which agrees with the experimental results (see Fig. 4.3(a) and (b)). Moreover, the leading pulse appears to have stronger intensity than the trailing pulse, which is also consistent with the observation in the experiment. The result suggests that, by experimentally resolving the dynamic of pulse temporal splitting, we are able to precisely estimate the MPI coefficient of the medium.

4.5 Conclusion

In sum, we have demonstrated time-resolved dynamics of pulse self-steepening and pulse temporal splitting in a single shot using B-FDSC. The result demonstrates that the revelation of pulse dynamics allows us to benchmark the MPI coefficient of bulk optical media. We performed a UPPE simulation to support the experimental results.

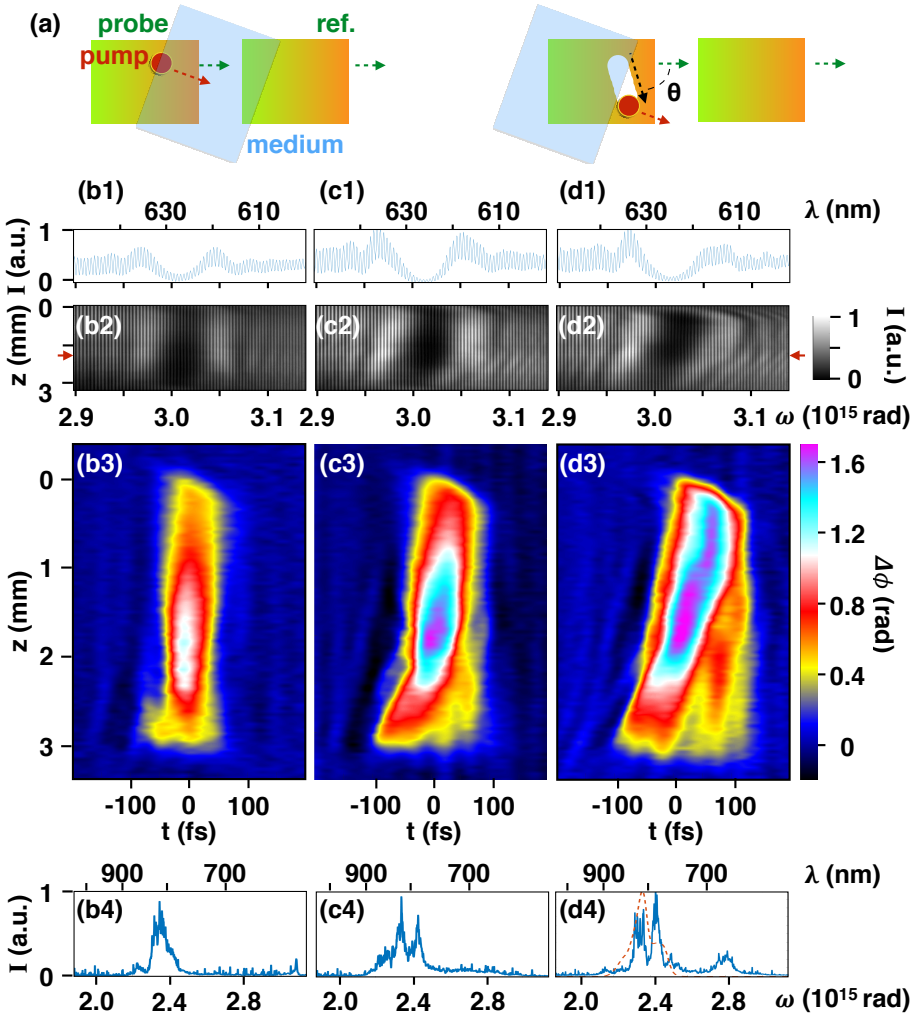

Figure 4.2: The experimental results. (a) The cartoon that demonstrates how the pump pulse imprints a phase streak on the probe pulse. (b) to (d) The data with different pump pulse energies, which are 0.9, 1.8, and 2.4 μJ respectively. (b1) to (d1) The line-out of the hologram data. (b2) to (d2) The raw hologram data. (b3) to (d3) The phase streaks extracted from the hologram data. Since the projection angle is close to 90° in the probe frame, the horizontal line-out represents the temporal profile of the pump pump pulse. (b4) to (d4) The spectra of the pump pulse after propagating through the glass sample. The red dashed line in (d4) is the spectrum of the exit pulse of the simulation with $\sigma_K = 6.72 \times 10^7$ s^{-1}[TW/cm^2]$^{-3}$.

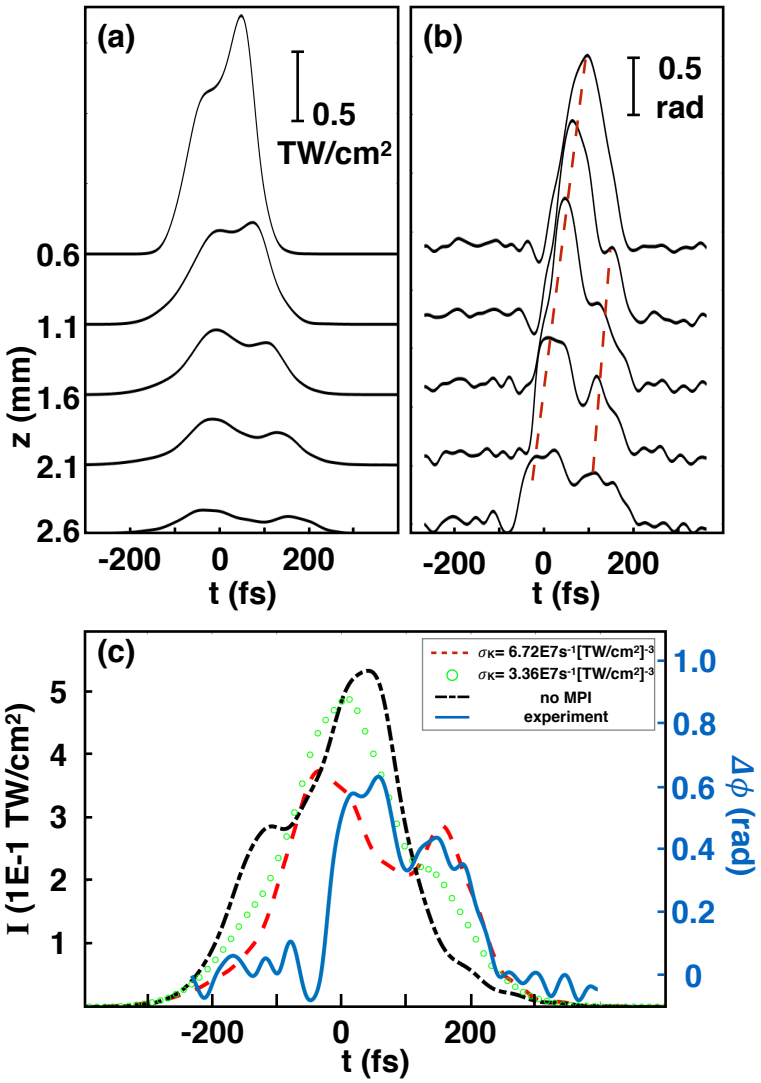

Figure 4.3: The result of the simulations and the comparison with the experimental data. (a) The pulse intensity on the propagation axis from the simulation where the MPI coefficient $\sigma_K = 6.72 \times 10^7$ $\mathrm{s}^{-1}[\mathrm{TW/cm}^2]^{-3}$. (b) The line-out of the phase streak of Fig. 4.2(d3). The red dashed lines highlight the trajectories of the pulses. (c) The pulse intensity on the propagation axis at $z = 2.56$ mm in the simulations with different MPI settings. The solid line is the line-out of the phase streak on Fig. 4.2(d3).

Chapter 5

Future Outlook

5.1 Faraday Rotation Diagnostic Improvement

Although we obtained signals of the plasma bubble evolution using Faraday rotation multiplexing, there are few things that we can do to improve the experimental setup.

1. We should use one wide beamsplitter for the beam sampler module. In the past experiment, the beam sampler module was constructed using two beamsplitters, but it was quite challenging to make sure that the surface of the two beamsplitters were perfectly aligned. The miss alignment of the two beamsplitter can affect the timing of the probe beams, especially the later probe beams (probe 3 and probe 4) because they don't propagate parallel to each other anymore. In fact, we may lose signals during the experiment because of the mis-alignment. To solve this problem, the quickest way is to buy one wide beamsplitter instead of using two small ones. It may affect the energy ratio between the probe beams. With two beamsplitters, we use a $80R/20T$ and a $70R/30T$, so the energy ratio between the first probe and the last probe is no larger than 67%. However, even with one beamsplitter, say we choose $80R/20T$, the

fourth probe still has 51% of the first probe, which is manageable for the cameras.

2. We should use high extinction ratio polarizer plates instead of polarizer cubes. The thick polarizer cubes distorted the anamorphic images too much that the resolution worsened drastically after we inserted the polarizers. To solve this problem, we can use the polarizer plates, which has less glass but still has high extinction ratio (1 : 1000).

3. If possible, we can squeeze the probe beams to increase the pulse intensity. The diameter of the probe beams is around 1 cm. The horizontal length of the probe beam makes time overlap less restrictive, but in most cases, the vertical length of the probe is too large for our purpose since we only need around 3 mm. On top of that, we saw strong scattered light from the main beam as background. To overcome the background and fully use the probe beams, we can squeeze the beam shape to elliptical to increase the pulse intensity.

5.2 Applying B-FDSC to LPAs

The prototype experiment of B-FDSC has demonstrated that the temporal resolution may be enough to resolve the dynamics of LPAs. However, to apply B-FDSC to LPAs, there are few things that we need to improve.

1. The energy of the probe beam in the prototype experiment was around 5 μJ after the short-pass filter, and the spectral range of the probe beam

was close to the scattered background from the laser plasma interaction. To overcome the problem, one can increase the energy of the probe by introducing more light to the supercontinuum generation process. One main issue of doing that is that when the intensity of the pulse is too strong, the broadened spectrum might be modulated and is not usable for the experiment. One can use a bigger beam spot or stretch the pulse length to tune the intensity for the broadening process.

2. Another way to overcome the background scattered light from the main beam is to double the frequency of the probe beam. The intensity of the spectrum-broaden beam might be too weak to induce second harmonic, and the bandwidth might be too broad for phase-matching, so one may need to double the frequency of the probe before the broadening process. We have tried to broaden the spectrum of the doubling pulse, but it was not successful mainly because the intensity of the doubling pulse was too weak. The profile of the frequency doubled pulse was too irregular that it couldn't focus into a nice spot, so one may need to send the beam through a pin hole after double the frequency.

Appendix 1

Faraday Rotation Diagnostics - Setup Procedure

1.1 Experimental Setup and preparation

1.2 imaging System

One challenge of applying Faraday rotation diagnostics to TX PW wakefield experiments was to acquire a wide horizontal field of view while maintaining a reasonable vertical resolution. The total propagation distance of the TX PW LPA is $\sim 7\ cm$, and the size of the rotation angle signal should be close to the plasma wavelength $\lambda_p \sim 40\ \mu m$. Since we did not know specifically where to probe the gas cell, we needed to cover as much longitudinal range as possible. Therefore, we established an anamorphic imaging system to demagnify the horizontal dimension to obtain wide field of view, but at the same time, magnify the vertical dimension to achieve a reasonable resolution.

The anamorphic imaging system consists of three lenses. Lens 1 is an objective lens with small f number to collect the light. Lens 2 is an achromatic cylindrical lens with long focal length, and Lens 3 is another achromatic cylindrical lens with short focal length. In wakefield 4.0 and 4.5, the lenses we used were a 15 cm achromatic spherical lens with 2" aperture, and two 1"

achromatic cylindrical lenses with 25 and 5 *cm* focal length respectively.

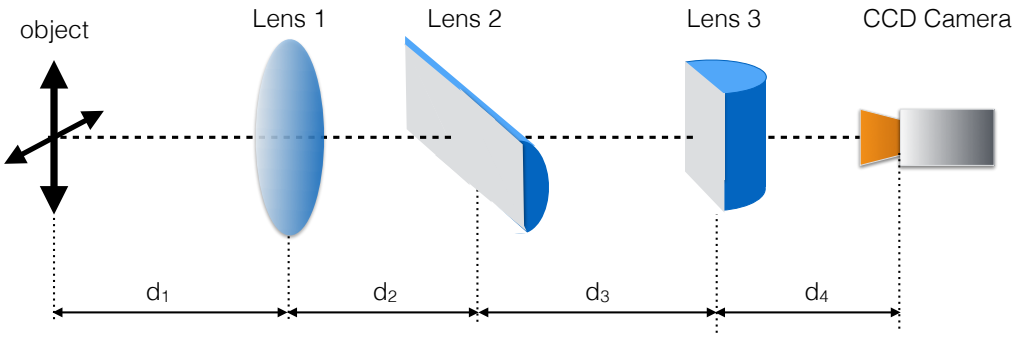

Figure 1.1: Schematic of the anamorphic setup.

The alignment procedure for setting up the anamorphic imaging system in the TX PW TC2 chamber is as follows:

1. Make sure the probe beam propagates along the centerline of the imaging system (see Figure 1.1). Since the imaging quality is highly sensitive to both the longitudinal and the transverse positions of the lenses, we used a cage system to ensure that the axis of the lenses are well aligned. Once the cage system is secured on the optics table, put a pinhole at the center line and align the probe beam. Note that the pointing of the probe beam can also affect the image quality, so it is essential to align the probe beam along the axis of the imaging system.

2. Turn on the He-Ne laser that propagates along the path of the main beam. Put a resolution target at the center of the chamber (or the

location that one wants to image), and make sure that the surface of the target is along the path of the He-Ne laser.

3. Setup Lens 1 (first achromatic spherical lens). The distance between the object and Lens 1 should be close to, but slightly longer than the focal length (f_1) to ensure an optimum aspect ratio of the final image (see Appendix **??**). Note that the object distance shouldn't be smaller than the focal length, otherwise the light will not focus to form an image.

4. Setup Lens 2 (first achromatic cylindrical lens). Lens 2 has longer focal length ($f_2 = 25\ cm$) and is used to image the vertical dimension, so the axis of the lens must be horizontal. The distance between the Lens 2 and Lens 1 (d_1) depends on the object distance. In principle, if the object distance is close to f_1, then d_1 should be close to the f_1 as well. One can put a piece of paper behind Lens 2 and look for an image with clear and sharp horizontal lines. Ideally, when $d_1 \sim f_1$, the image plane, that is, the distance between Lens 2 and the ideal image plane, should be close to f_2.

5. Setup Lens 3 (second achromatic cylindrical lens). Lens 3 has shorter focal length (f_3) and is used to image the horizontal dimension, so the axis of the lens should be vertical. If $d_1 \sim f_1$, then d_3 should be close to $f_2 - f_3$, and $d_4 \sim f_3$.

6. Setup a CCD camera to capture the image. Position the camera to acquire a reasonable image. There are two ways to , and adjustadjust

the lenses. One way is to fix the position of Lens 1. Move Lens 2 to optimize the horizontal lines. Once the horizontal lines are optimized, adjust Lens 3 to optimize the vertical lines. Repeat the adjustment between the camera, Lens 2 and Lens 3. if necessary. Another way of finding the best image is to fix the distance (d_3) between Lens 2 and Lens 3, and move Lens 1 and the camera to find the best image. The image quality is not sensitive to d_2 but is highly sensitive to d_1 and d_4. Since we want the maximum aspect ratio, d_3 should be close to $f_2 - f_3$ in both methods. Ideally, the aspect ratio should be close to f_3/f_2 (See Figure 1.2).

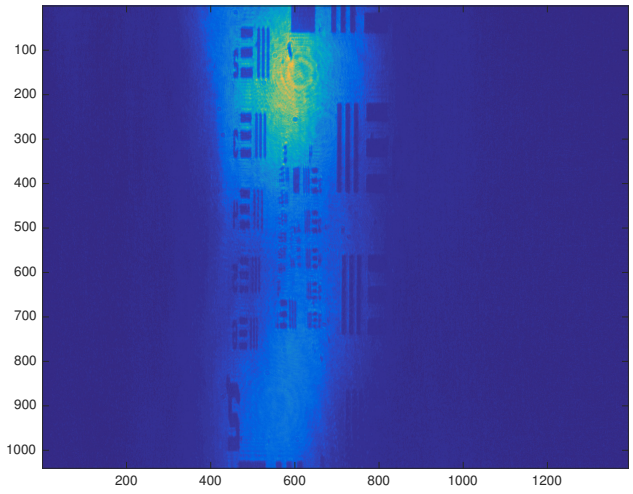

Figure 1.2: Anamorphic image of a resolution target.

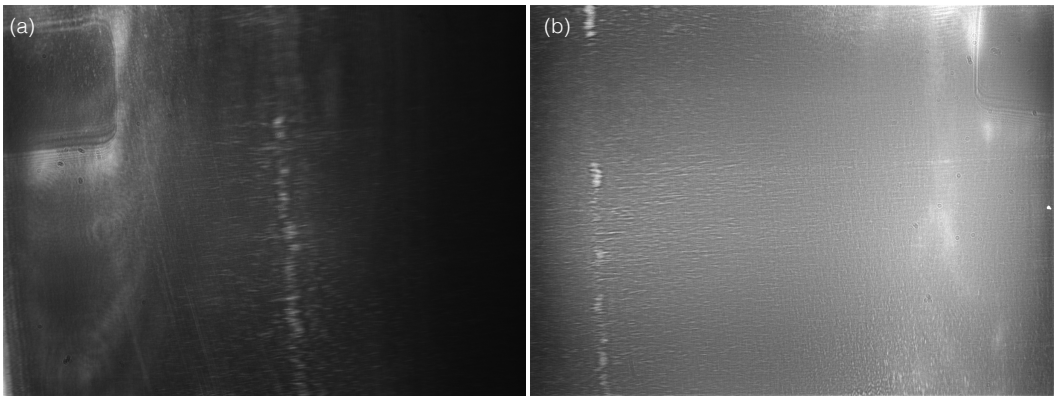

Figure 1.3: Examples of rod images for image overlapping calibration. (a) and (b) are the images of camera 1 and camera 2 respectively.

1.3 Camera Images Overlapping

To compare the images of the two cameras, We calibrated the location of the images. To do this, we put an iron rod inside the gas cell, and used the tip of the rod as a standard point to mark the position of the images. The position of the images on the two cameras does not need to be exact, but the overlapping area needs to at least cover the region of interest.

Note that for anamorphic imaging, the aspect ratio will be different with or without propagation through the beamsplitter, which makes it difficult to overlap the images on the two camera. In order to remove the defect caused by the beamsplitter, put a substrate (e.g. a window with the same material and same thickness of the beamsplitter) on the path of the reflected beam.

1.4 Rotation Angle Extraction

For a sensitive, low-background measurement of the rotation angle, we use two cameras with two polarizers in the front (See Figure **??**). The polarizers were rotated with biased angles so that the region where the polarization was rotated by Faraday effect will be bright on one camera and dark on the other. By dividing the images of the two cameras, one can extract the rotation angle.

The intensity transmitted through the polarizers can be written as

$$I_{i,0}y, z) = I_0(y, z) \cdot T_i(1 - \alpha_i \cdot cos^2(\phi_{rot}(y, z) - \theta_i))$$

, where $I_{i,0}$ $(i = 1, 2)$ is the intensity of the light transmit through of polarizer 1 and polarizer 2, I_0 is the original intensity, T_i is transmission/reflection ratio of the beam splitter, the α_i is the extinction ratio of the polarizers, ϕ_{rot} is the rotation angle, and θ_i is the biased angle of the polarizer, which should be close to the expected rotation angle.

As we discussed in section **??**, the intensities actually captured by the cameras may vary because of the efficiency. Therefore, $I_1 = R_1 \cdot I_{i,0}$ and $I_2 = R_2 \cdot I_{2,0}$, where R_1 and R_2 are the efficiencies of camera 1 and 2 respectively.

The procedure of the angle extraction is the following:

1. The images captured by the two cameras may have some background lights and scattered light from the main beam, so one may need to use

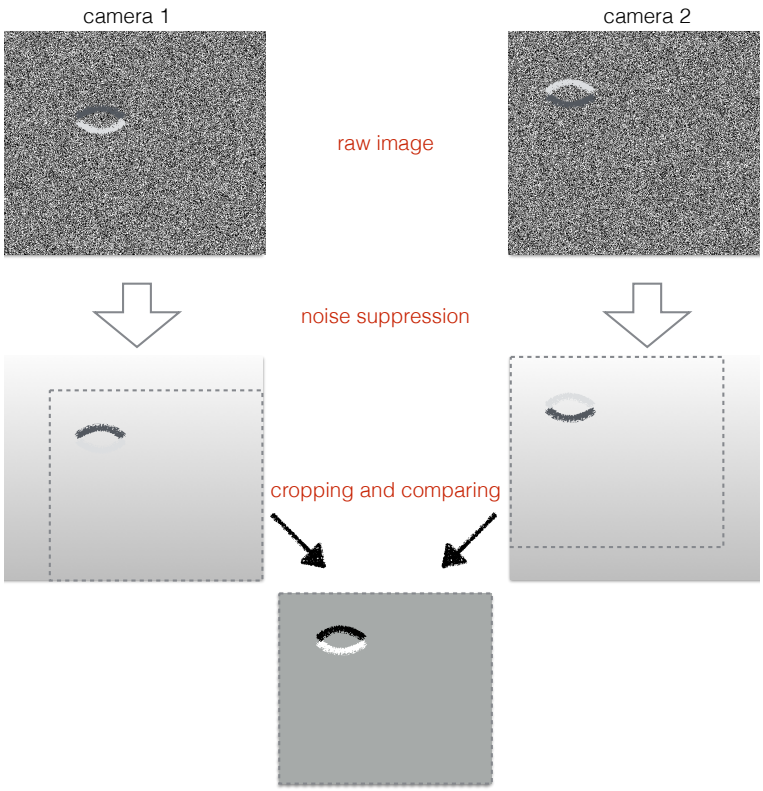

Figure 1.4: The fitting curve of the calibrations of (a), polarizer 1 and (b), polarizer 2.

spatial filter (e.g. Fourier transform) to suppress the noise on the images.

2. Overlap the images according to the reference point identified by looking at the images of the rod (see section **??**). One may need to crop the images to the same size. (see Figuer1.4)

3. Compare the two cropped images and obtain the ration ($R_0(y,z) = I_1(y,z)/I_2(y,z)$). The ratio where there was no signal should be 1. That is, the area where there is no magnetic field on the two images should

be the same. One may need to introduce a coefficient to weigh the ratio and let the background level close to 1. In other words, find a constant Γ to let $R(y,z) = \Gamma \cdot I_1(y,z)/I_2(y,z)$ has a reasonable background level.

4. Find the rotation angle ($\phi_{rot}(y,z)$) by solving

$$R(y,z) = \Gamma \cdot \frac{(1 - \alpha_1 \cdot cos^2(\phi_{rot}(y,z) + \theta_1))}{(1 - \alpha_2 \cdot cos^2(\phi_{rot}(y,z) + \theta_2))}$$

, where $R(y,z)$ is the ratio after background adjustment, Γ is the background suppression constant, $\phi_{rot}(y,z)$ is the rotation angle that we want to know, and θ_1 and θ_2 are the biased angles of the polarizers. Note that there might be multiple solutions for $\phi_{rot}(y,z)$ for every point (y,z), and the correct solution should be close to the expected values.

1.5 Rotation Angle Estimation

Before we applied the Faraday rotation diagnostics, we had to estimate value of the expected rotation angle, which was necessary for the setup. The rotation angle of the Faraday effect can be expressed as

$$\phi_{rot} = \frac{e}{2m_e c n_c} \int_l n_e \mathbf{B}_\varphi \cdot d\mathbf{s}$$

where e is electron charge, m_e is electron mass, c is speed of light, n_e is plasma density, and n_c is the critical density (here, $n_c = 1.77 \times 10^{20}\ cm^{-3}$) respectively. $\mathbf{B}_\varphi$ is the azimuthal magnetic field, and $d\mathbf{s}$ is the path element along the path of the probe beam through the plasma.

ϕ_{rot} can be obtained by running computer simulations, which may take several days to get the result. We can also use a simple model to roughly estimate ϕ_{rot}.

The assume the plasma density n_e can be written in cylindrical coordinate as

$$n_e = n_0 \cdot exp(-(r - r_b(\xi))/\sigma_p)$$

where n_0 is the peak value of dense electron sheath wall of the plasma bubble. ξ is the comoving frame of the plasma bubble, and σ_p is the characteristic thickness of the bubble sheath wall. Note that since the laser beam in the bubble essentially blow out all the electrons in the bubble, we assume the plasma density is zero when $r < r(\xi)$.

As for the magnetic field , since the probe beam propagates transversely to the plasma bubble, $\mathbf{B} \cdot d\mathbf{s}$ is equivalent to $\mathbf{B}_\varphi \cdot d\mathbf{s}$, which means we can focus on the the azimuthal component of the magnetic field. B_φ is contributed from two sources: the electron beams and the displacement current J_z of the plasma bubble sheath wall. However, since the magnetic field induced by J_z is around 7 times weaker than that is induced by the electron beams, we will ignore J_z in the rough estimation of ϕ_{rot}.

The magnitude of $\mathbf{B}_\varphi$ induced by the electron beams can be written as $B_\varphi = \frac{\mu_0 c}{4\pi} \frac{q|\boldsymbol{\beta}|}{|\mathbf{R}|^2\sqrt{1-|\boldsymbol{\beta}|^2 sin^2\theta}}$. Here, $\mathbf{R}$ is the displacement from the electrons to the field, $\boldsymbol{\beta}$ is the velocity of the electrons normalized by the speed of light, θ

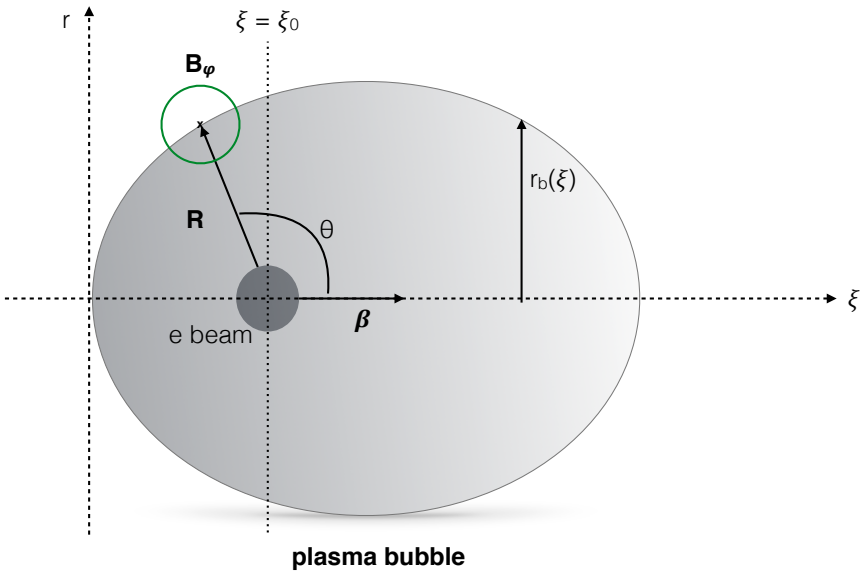

Figure 1.5: Schematic of the magnetic field induced by the electron beams.

is the angle between $\mathbf{R}$ and $\boldsymbol{\beta}$, and q is the charge of the electron bunch (see Figure 1.5). When $\theta = 90°$, the azimuthal magnetic field becomes

$$B_{\varphi,\perp} = B_{\varphi}(\theta = 90°) = \frac{\mu_0 c}{4\pi} \frac{q\gamma}{|\mathbf{R}|^2}.$$

To simplify the problem, we consider only the ϕ_{rot} on the plane of the center of the electron beam. That is, we calculate ϕ_{rot} on the plane $\xi = \xi_0$.

Bibliography

[1] T. Tajima and J. Dawson. Laser electron accelerator. *Physics Review Letter*, 43:267–270, 1979.

[2] X. Wang, R. Zgadzaj, N. Fazel, Z. Li, S. A. Yi, X. Zhang, W. Henderson, Y. Y. Chang, R. Korzekwa, H. E. Tsai, C. H. Pai, H. Quevedo, G. Dyer, E. Gaul, M. Martinez, A. C. Bernstein, T. Borger, M. Spinks, M. Donovan, V. Khudik, G. Shvets, T. Ditmire, and M. C. Downer. Quasi-monoenergetic laser-plasma acceleration of electron to 2 gev. *Nature Communication*, 4:1988, 2013.

[3] H. E. Tsai, X. Wang, J. M. Shaw, Z. Li, A. V. Arefiev, X. Zhang, R. Zgadzaj, W. Henderson, V. Khudik, G. Shvets, and M. C. Downer. Compact tunable compton x-ray source from laser-plasma accelerator and plasma mirror. *Physics of Plasmas*, 22:023106, 2015.

[4] A. Pukhov and J. Meyer-Ter-Vehn. Laser wake field acceleration: the highly non-linear broken-wave regime. *Applied Physics B*, 74:355–361, 2002.

[5] N. Barov, J. B. Rosenzweig, M. C. Thompson, and R. B. Yoker. Energy loss of a high-charge bunched electron beam in plasma: Analysis. *Physical Review Special Topics - Accelerators and Beams*, 7:60–70, 2004.

[6] K. Lotov. Blowout regimes of plasma wakefield acceleration. *Physical Review E*, 69:046405, 2004.

[7] I. Kostyukov, A. Pukhov, and S. Kiselev. Phenomenological theory of laser-plasma interaction in "bubble" regime. *Physics of Plasmas*, 11:5256, 2004.

[8] W. Lu, C. Huang, M. Tzoufras, F. S. Tsung, W. B. Mori, and T. Katsouleas. A nonlinear theory for multidimensional relativistic plasma wave wakefields. *Physics of Plasmas*, 13:056709, 2006.

[9] A. G. R. Thomas. Scalings for radiation from plasma bubbles. *Physics of Plasmas*, 17:056708, 2010.

[10] C. Benedetti, C. B. Schroeder, E. Esarey, F. Rossi, and W. P. Leemans. Numerical investigation of electron self-injection in the nonlinear bubble regime. *Physics of Plasmas*, 20:103108, 2013.

[11] D. H. Froula, C. E. Clayton, T. Doppner, R. A. Fonseca, K. A. March, C. J. Barty, L. Divol, S. H. Glenzer, C. Joshi, W. Lu, S. F. Martins, P. Michel, W. Mori, J. P. Palastro, B. B. Pollock, A. Pak, J. E. Ralph, J. S. Ross, C. Sider, L. O. Silva, and T. Wang. Measurements of the critical power for self-injection of electrons in a laser wakefield accelerator. *Physical Review Letters*, 103:215006, 2009.

[12] S. P. D. Mangles, G. Genoud, M. S. Bloom, M. Burza, Z. Najmudin, A. Persson, K. Svensson, A. G. R. Thomas, and C.-G. Wahlstrom. Self-

injection threshold in self-guided laser wakefield accelerators. *Physical Review Special Topics - Accelerators and Beams*, 15:011302, 2012.

[13] S. Kalmykov, S. A. Yi, V. Khudik, and G. Shvets. Electron self-injection and trapping into an evolving plasma bubble. *Physical Review Letters*, 103:135004, 2009.

[14] S. Y. Kalmykov, S. A. Reed, S. A. Yi, A. Beck, A. F. LIfschitz, X. Davonie, E. Lefebvre, V. Khudik, G. Shvets, P. Dong, X. Wang, D. Du, S. Bedacht, Y. Zhao, W. Henderson, A. Bernstein, G. Dyer, M. Martinez, E. Gaul, T. Dimire, and M. C. Downer. Laser wakefield electron acceleration on texas petawatt facility: Towards multi-gev electron energy in a single self-guided stage. *High Energy Density Physics*, 6:200–206, 2010.

[15] J. Faure, Y. Glinec, J. J. Santos, F. Ewald, J.-P. Rousseau, S. Kiselev, A. Pukhov, T. Hosokai, and V. Malka. Observation of laser-plasma shortening in nonlinear plasma wave. *Physical Review Letters*, 95:205003, 2005.

[16] W. Lu, M. Tzoufras, C. Joshi, F. S. Tsung, W. B. Mori, J. Vieira, R. A. Fonseca, and L. O. Silva. Generating multi-gev electron bunches using single stage laser wakefield acceleration in a 3d nonlinear regime. *Physical Review Special Topics - Accelerators and Beams*, 10:061301, 2007.

[17] J. A. Stamper and B. H. Ripin. Faraday-rotation measurements magnetic fields in laser-produced plasmas. *Physical Review Letters*, 34:138, 1975.

[18] M. C. Kaluza, H.-P. Schlenvoigt, S. P. D. Mangles, A. G. R. Thomas, A. E. Dangor, H. Schwoeger, W. B. Mori, Z. Najmudin, and K. M. Krushelnick. Measurement of magnetic-field structure in a laser-wakefield accelerator. *Physical Review Letters*, 105:115002, 2010.

[19] A. Flacco, J. Vieira, A. Lifschitz, F. Sylla, S. Kahaly, M. Veltcheva, L. O. Silva, and V. Malka. Persistence of magnetic field driven by relativistic electrons in a plasma. *Nature Physics*, 11:409–413, 2015.

[20] A. Buck, M. Nicolai, K. Schmid, C. M. S. Sears, A. Savert, M. Mikhailova, F. Krausz, M. C. Kaluza, and L. Veisz. Real-time observation of laser driven electron acceleration. *Nature Physics*, 7:543–548, 2011.

[21] C. W. Sider, S. P. Le Blanc, D. Fisher, T. Tajima, and M. C. Downer. Laser wakefield excitation and measurement by femtosecond longitudinal interferometry. *Physics Review Letter*, 76(19):3570–3573, 1996.

[22] N. H. Matlis, S. Reed, S. S. Bulanov, V. Chvykov, G. Kalintchenko, T matsuoka, P. Rousseau, V. Yanovsky, A. Maksimchuk, S. Kalmykov, G. Shvets, and m. C. Downer. Snapshots of laser wakefield. *Nature Physics*, 2:749–753, 2006.

[23] P. Dong, S. A. Reed, S. A. Yi, S. Kalmykov, G. Shvets, and M. C. Downer. Formation of optical bullets in laser-driven plasma bubble accelerators. *Physical Review Letters*, 13:134801, 2010.

[24] Z. Li, R. Zgadzaj, X. Wang, S. Reed, P. Dong, and M. Downer. Frequency-domain streak camera for ultrafast imaging of evolving light-velocity objects. *Optics Letters*, 35:4087–9, 2010.

[25] Z. Li, H. E. Tsai, X. Zhang, C. H. Pai, Y. Y. Chang, R. Zgadzaj, X. Wang, V. Khudik, G. Shvets, and M. C. Downer. Single-shot visualization of evolving laser wakefield using an all-optical streak camera. *Physical Review Letters*, 113:085001, 2014.

[26] A. Savert, S. P. D. Mangles, M. Schnell, E. Siminos, J. M. Cole, M. Leier, M. Reuter, M. B. Schwab, M. Moller, K. Poder, O. Jackel, G. G. Paulus, C. Spielmann, S. Skupin, Z. Najmudin, and M. C. Kaluza. Direct observation of the injection dynamics of a laser wakefield accelerator using few-femtosecond shadowgraphy. *Physical Review Letters*, 115:055002, 2015.

[27] Z. Li. Single-shot visualization of evolving , light-speed refractive index structures. *UT Austin Dissertation*, 2014.

[28] S. Y. Kalmykov, A. Beck, S. A. Yi, V. N. Khudik, M. C. Downer, E. Lefebvre, B. A. Shadwick, and D. P. Umstadter. Electron self-injection into an evolving plasma bubble: Quasi-monoenergetic laser-plasma acceleration in the blowout regime. *Physics of Plasmas*, 18:056704, 2011.

[29] S. A. Yi, V. Khudik, C. Siemon, and G. Shvets. Analytic model of electromagnetic fields around a plasma bubble in the blow-out regime. *Physics of Plasmas*, 20:013108, 2013.

[30] A. E. Broderick and A. Loeb. Signatures of relativistic helical motion in the rotation measures of active galactic nucleus jets. *The Astrophysical Journal*, 703:L104–L108, 2009.

[31] C. Geddes, C. Toth, J. Van Tilborg, E. Esarey, C.B. Schroeder, D. Bruhwiler, C. Nieter, J. Cary, and W.P. Leemans. High-quality electron beams from a laser wakefield accelerator using plasma-channel guiding. *Nature*, 401:538–541, 2004.

[32] G. Sun, E. Ott, Y. Lee, and P. Guzdar. Self-focusing of short intense pulses in plasmas. *Physics of Fluids*, 30:526, 1987.

[33] C.G.R. Geddes, Cs. Toth, J. van Tilborg, E. Esarey, C.B. Schroeder, J. Cary, and W.P. Leemans. Guiding of relativistic laser pulses by preformed plasma channels. *Physical Review Letters*, 95(145002):145002, 2005.

[34] E. Esarey, C.B. Schroeder, and W.P. Leemans. Physics of laser-driven plasma-based electron accelerators. *Review of Modern Phyiscs*, 81:1229–1285, 2009.

[35] C.J. Zhang, J.F. Hua, Y. Wan, C.-H. Pai, B. Guo, J. Zhang, Y. Ma, F. Li, Y.P. Wu, H.-H. Chu, Y.Q. Gu, X.L. Xu, W.B. Mori, C. Joshi, J. Wang, and W. Lu. Femtosecond probing of plasma wakefields and observation of the plasma wake reversal using a relativistic electron bunch. *Physical Review Letters*, 119(064801), 2017.

[36] B. Walton, A.E. Dangor, S.P.D. Mangles, Z. Najmudin, K. Krushenlnick, A.G.R. Thomas, S. Fritzler, and V. Malka. Measurements of magnetic field generation at ionization fronts from laser wakefield acceleration experiments. *New Journal of Physics*, 15(025034), 2013.

[37] E. Gaul, T. Toncian, M. Martinez, J. Gordon, M. Spinks, G. Dyer, N Truong, C. Wagner, G. Tiwari, M.E. Donovan, T. Ditmire, and B.M. Hegelich. Improved pulse contrast on the texas petawatt laser. *Journal of Physics: Conference Series*, 717(012092):012092, 2016.

[38] A.G.R. Thomas, S.P.D. Mangles, Z. Najmudin, M.C. Kaluza, C.D. Murphy, and K. Krushelnick. Measurements of wave-breaking radiation from a laser-wakefield accelerator. *Physics Review Letters*, 98(054802):054802, 2007.

[39] X. Yang, E. Brunetti, D. Reboredo Gil, G. H. Welsh, F. Y. Li, S. Cipiccia, B. Ersfeld, D. W. Grant, P. A. Grant, M. R. Islam, M. P. Tooley, G. Vieux, S. M. Wiggins, Z. M. Sheng, and D. A. Jaroszynski. Three electron beams from a laser-plasma wakefield accelerator and the energy apportioning question. *Scientific Reports*, 7:1–10, 2017.

[40] P. Mora and T.M. Antonsen Jr. Kinetic modeling of intense, short laser pulses propagating in tenuous plasmas. *Physics of Plasmas*, 4:217–229, 1997.

[41] J. H. Marburger. Self-focusing: Theory. *Progress in Quantum Electronics*, pages 35–110, 1975.

[42] A. Gaeta. Catastrophic collapse of ultrashort pulses. *Physical Review Letters*, 84:3582–5, 2000.

[43] P.Chernev and V. Petrov. Self-focusing of light pulses in the presence of normal group-velocity dispersion. *Optics Letters*, 17(3):172, 1992.

[44] S. Diddams, H. Eaton, A. Zozulya, and T. Clement. Amplitude and phase measurements of femtosecond pulse splitting in nonlinear dispersive media. *Optics Letters*, 23(5):379–81, 1998.

[45] J. Ranka, R. Schirmer, and A. Gaeta. Observation of pulse splitting in nonlinear dispersive media. *Physical Review Letters*, 77(18):3783–3786, 1996.

[46] S. Tzortzakis, L. Sudrie, M. Franco, B. Prade, and A. Mysyrowicz. Self-guided propagation of ultrashort ir laser pulses in fused silica. *Physics Review Letters*, 87(21):19–22, 2001.

[47] Z. Li, R. Zgadzaj, X. Wang, Y.Y. Chang, and M. Downer. Single-shot tomographic movie of evolving light-velocity objects. *Nature Communications*, 5:3085, 2014.

[48] K. Kim, I. Alexeev, and H. Milchberg. Single-shot supercontinuum spectral interferometry. *Applied Physics Letters*, 81:4124–4126, 2002.

[49] E. Tokunaga, A. Terasaki, and T. Kobayashi. Femtosecond continuum interferometer for transient phase and transmission spectroscopy. *Journal of the Optical Society of America B*, 13:496, 1996.

[50] C.H. Lu, Y.J. Tsou, H. Y. Chen, B.H. Chen, Y.C. Cheng, S. D. Yang, M. C. Chen, C.C. Hsu, and A. H. Kung. Generation of intense supercontinuum in condensed media. *Optica*, 1:10–12, 2014.

[51] D. Anderson and M. Lisak. Nonlinear asymmetric self-phase modulation and self-steepening of pulses in long optical waveguides. *Physical Review A*, 27:1393–1398, 1983.

[52] J. Rothenberg. Space-time focusing: breakdown of the slowly varying envelope approximation in the self-focusing of femtosecond pulses. *Optics Letters*, 17:1340–1342, 1992.

[53] A. Couairon, E. Brambilla, T. Corti, D. Majus, O. de J. Ramírez-Góngora, and M. Kolesik. Practitioner's guide to laser pulse propagation models and simulation. *Eur. Phys. J. Special Topics*, 199:5–76, 2011.

[54] C. Schaffer, A. Brodeur, and E. Mazur. Laser-induced breakdown and damage in bulk transparent materials induced by tightly focused femtosecond laser pulses. *Measurement Science and Technology*, 12:1784–1794, 2001.

[55] Q. Sun, H. Jiang, Y. Liu, Z. Wu, H. Yang, and Q. Gong. Measurement of the collision time of dense electronic plasma induced by a femtosecond laser in fused silica. *Optics Letters*, 30:320–322, 2005.

[56] A. Couairon and A. Mysyrowicz. Femtosecond filamentation in transparent media. *Physics Reports*, 30:47–189, 2007.

[57] I. Kostyukov, E. Nerush, A. Pukhov, and V. Seredov. Electron self-injection in multidimensional relativistic-plasma wake fields. *Physical Review Letters*, 103:175003, 2009.

[58] W. Lu, C. Huang, M. Zhou, W. B. Mori, and T. Katsouleas. Nonlinear theory for relativistic plasma wakefield in the blowout regime. *Physics Review Letter*, 96(165002):165002, 2006.